High Entropy Alloys for Nuclear Fusion Applications

André Felipe de Jesus Lopes Ruza

Thesis to obtain the Master of Science Degree in

Materials Engineering

Supervisor:
Dr. Marta Dias

Co-supervisor:
Dr. António Gonçalves

Examination Commitee

Chairperson:
Prof. Pedro Amaral

Committee:
Dr. Rui Silva

November of 2017

Agradecimentos

Quero agradecer à minha orientadora Doutora Marta Dias, pela oportunidade de participar num projeto tão interessante e motivador, e por ainda me apoiar na preparação desta tese.

Ao meu coorientador, Doutor António Gonçalves pela disponibilidade e sugestões.

Especial atenção aos colegas que conheci no CTN e com os quais aprendi imenso. Norberto Catarino pelo constante apoio e paciência e à Filomena Batista por toda ajuda prestada.

O trabalho recebeu ainda o apoio indispensável de Andrei e Magdalena Galatanu, que disponibilizaram o seu equipamento e tempo para ajudar na preparação de amostras.

Muito grato pela amizade de todos os que mais perto ou mais longe me acompanharam estes anos todos, quer antigas amizades como Rui Carreira, Pedro Gaspar e Ricardo Branco, como novas que fui realizando no percurso académico. Em especial à Rita Faustino, sem ela não teria tido a oportunidade de fazer esta tese e pela companhia no CTN.

À minha família, o meu pai, Vitor dos Santos, a minha mãe, Aura Villegas e irmã, Diana Ruza, que sempre me acompanharam e estiveram presentes proporcionando-me todas as possibilidades.

Agradeço à minha namorada, Filipa Alves, pela ajuda, paciência e motivação que sempre me prestou.

Resumo

Num reator de fusão nuclear, “tokamak”, o diversor está sujeito a um elevado fluxo térmico. Tungsténio foi escolhido como o material de primeira parede mais próximo do plasma e uma liga de CrCuZr funcionará como dissipador de calor. A dissimilaridade entre os dois materiais: a elevada temperatura de transição dúctil-frágil do tungsténio e a baixa temperatura de trabalho do CuCrZr, levam à extração do calor menos eficiente e a um tempo de vida reduzido. Neste trabalho, inicia o estudo em ligas de alta entropia numa tentativa de procurar por um material de união adequado a ser usado como barreira térmica para suavizar a transição térmica entre ambos.

As ligas de alta entropia são parte de uma nova área de metalurgia. Esta refere-se a ligas que contenham pelo menos 5 elementos, em geral metálicos, com composições que vão desde 5 a 35 em percentagem atómica. O interesse aumenta por ter sido verificado, para várias composições, a formação de soluções sólidas simples metastáveis com propriedades que prometem bons resultados, no que toca ao seu uso em reatores de fusão como barreiras térmicas. Como por exemplo, alta dureza e resistência a elevadas temperaturas, baixas difusividades térmicas e resistência à radiação.

Foram estudados os sistemas CrCuFeMoTi e CrCuFeTiV. O efeito composicional foi identificado ao produzir 6 amostras em vácuo por forno de arco. Três de CrCu$_x$FeMoTi e outras três de CrCu$_x$FeTiV, em que o x representa diferentes proporções molares de cobre. O método de produção foi estudado ao produzir uma única amostra equimolar, CrCuFeTiV, por “mechanical alloying”, durante 20 horas a 400 rpm, seguido de “spark plasma sintering” a uma pressão de 65 MPa a 900 ºC. As amostras foram caracterizadas com microscopia eletrónica de varrimento, difração de raios-X e difração de eletrões retrodifundidos. As amostras produzidas por forno de arco revelaram microstructuras complexas com muitas fases, tendo os dois sistemas o mesmo tipo de fase de Laves como matriz, e outras fases ricas em cobre e titânio distribuídas pela estrutura. O sistema CrCu$_x$FeMoTi revelou elevada segregação de molibdénio. No sistema de CrCu$_x$FeTiV uma solução sólida BCC foi identificada, mas que ainda assim não foi capaz de dissolver na totalidade os elementos. A amostra sinterizada possuía uma estrutura mais simples, com zonas ricas em cobre e uma solução sólida FCC como matriz juntamente com outra fase não identificada. Iões de árgon foram usados para similar as condições de implantação da amostra.

Resultados sugerem que o controlo de cobre e titânio são a chave para obter soluções sólidas e que a melhoria do processo de moagem pode melhorar as condições para promover estruturas simples

Palavras-chave: liga de alta entropia; “mechanical alloying”; forno de arco; microestrutura; irradiação; sinterização por faísca de plasma.

Abstract

In a tokamak, nuclear fusion reactor, the divertor is subjected to a high heat flux. Tungsten has been chosen as its plasma facing material and CuCrZr alloy was chosen as the heat sink material. The dissimilarity between both materials: the high ductile-brittle transition temperature of tungsten and the low service temperature of CuCrZr, will lead to a less efficient heat extraction and shorter service life time. In this work, study begins on high-entropy alloy system in an attempt to search for an alternative bond coat material for thermal barriers to smooth the thermal transition.

High entropy alloys are part of a novel area of metallurgy concerning alloys containing at least 5 elements with compositions ranging from 5 at.% to 35 at.%. The interest arises as it has been verified, for plenty compositions, the formation of metastable simple solid solutions with promising properties, pertaining their use in nuclear fusion as thermal barriers, such as high strength and hardness at high temperature, low thermal diffusivity and high radiation resistance.

The CrCuFeMoTi and CrCuFeTiV systems were studied. The compositional effect was identified by producing 6 samples by vacuum arc melting. Three of $CrCu_xFeMoTi$ and three other of $CrCu_xFeTiV$, where x denotes the varying copper molar ratio. The production method was evaluated by producing a single CrCuFeTiV sample by mechanical alloying, for 20 hours at 400 rpm, followed by spark plasma sintering at a pressure of 65 MPa at 900 ºC. The samples were characterized by SEM, XRD and EBSD analysis. The samples produced by arc melting revealed complex multiphasic microstructures, having both systems the same type of Laves matrix phase and other copper and titanium rich phases distributed throughout the matrix. The $CrCu_xFeMoTi$ revealed a heavy segregation of molybdenum, likely related to its higher melting temperature and binary enthalpy of mixing with the other elements. In the $CrCu_xFeTiV$ system a BCC solid solution was identified, yet it did not fully dissolve the remaining elements. The sintered CrCuFeTiV possessed a much simpler structure, with copper rich regions, and an FCC solid solution as the matrix, with another unidentified phase. Argon ions were used to simulate conditions of irradiation in the sample.

Results suggest that control of copper and titanium content are key to obtain solid solutions and that improvement of milling process can enhance the creation of simple structures.

Keywords: high entropy alloy; mechanical alloying; vacuum arc melting; microstructure; irradiation; spark plasma sintering.

Contents

List of figures

List of tables

Abbreviations

ALD	Atomic layer deposition
AM	Arc melt
BCC	Body centered cubic
BMG	Bulk metallic glasses
BPR	Ball to powder ratio
BSE	Backscattered electrons
CALPHAD	CALculations of PHAse Diagrams
DBTT	Ductile to brittle transition
DEMO	Demonstration fusion plant
DPA	Displacements per atom
EBSD	Electron backscatter diffraction
EDS	Energy dispersive spectroscopy
FCC	Face centered cubic
FGM	Functionally graded materials
GXRD	Grazing X-ray diffraction
HC	Hexagonal compact
HEA	High entropy alloy
HIP	Hot-isostatic pressing
H-R	Hume-Rothery
ICDD	International center for diffraction data
ITER	International thermonuclear experimental reactor
LENS	Laser enhanced net shape
MA	Mechanical alloying
MAD	Mean angular deviation
MBE	Molecular beam epitaxy
OPS	Silica oxide polishing suspension
PCA	Process control agent
PKA	Primary knock-on atom
PLD	Pulse laser deposition
PXRD	Powder X-ray diffraction
SE	Secondary electrons
SEM	Scanning electron microscopy
SGR	Space group

SPS	Spark plasma sintering
VEC	Valence electron concentration
VHP	Vacuum hot pressing
XRD	X-ray diffraction

List of symbols

H_{ij}	Binary enthalpy of mixture
T_m	Melting temperature
X_i	Atomic percentage of species *i*
c_i	Atomic percentage of component *i*
c_j	Atomic percentage of component *j*
r_i	Atomic radius of species *i*
χ_i	Pauling electronegativity of component *i*
ΔH_f	Enthalpy of fusion
ΔS_{conf}	Configurational entropy
ΔG	Gibbs free energy
ΔH	Enthalpy of mixing
$\Delta \chi$	Pauling electronegativity of system
Ω	Ratio of entropy contribution to enthalpy contribution at the melting temperature
C	Number of components
F	Degrees of freedom
P	Maximum number of possible phases
R	Gas constant
S	Entropy
T	Absolute temperature
k	Boltzmann constant
n	Number of atomic species in an alloy
δ	Atomic size difference factor
ω	Randomness measurement

1. Introduction

The advances in producing clean energy using nuclear fusion reaction facilities are limited by materials availability for this high-performance application. More specifically the dissimilarity between the materials applied in the divertor, a region exposed to high heat flux. Tungsten has been chosen as its plasma facing material and CuCrZr alloy was chosen as the heat sink material. The high ductile-brittle transition temperature of tungsten and low service temperature of CuCrZr, will lead to a less efficient heat extraction and lower service life time of the part. The use of an adequate interlayer material, between the tungsten and the copper alloy, as a thermal barrier to smooth the thermal transition by maintaining the outer region at high temperature and the inner at lower temperature, adequate to the chosen materials, is from our point of view a high research focus.

This thesis represents the beginning of a study to find suitable materials to be used as thermal barrier materials in fusion reactors. Issues in the industries can also be seen as opportunities to study new materials to look for new and improved properties. High entropy alloys present themselves as suitable candidates to fill this gap. For these two systems never studied before, CrCuFeMoTi and CrCuFeTiV are taken as the basis for the study.

The results are divided in two major sections related to the production method of the studied compositions. One part is related to the samples produced by vacuum arc melting, melting and solidification routes. A comparison between the compositional effect within the same technique is noted. The other focus solid-state processing, mechanical alloying and sintering. It draws a parallel with the previous production method and analyses the obtained results.

Overall the document is divided in seven sections. Beginning with the introduction in Section 1 and followed by Section 2 – Background, which provides information on the task at hand in the nuclear reactor and gives the reader an understanding on the basics high entropy alloys. Section 3 – Techniques and Procedures explains the techniques and denotes how the experimental work was performed. The two next sections focus on the results and discussion for the molten samples, Section 4 – Liquid Route and for the sintered sample, Section 5 – Solid Route. To finish, conclusions are drawn in Section 6 – Conclusions and Future Work.

2. Background

This section will introduce concepts necessary to grasp the scope of this work. Issues that are present within the fusion reactor project give rise to the motivation of this work. The state of the art of current interlayer technology will be reviewed followed by a brief review of high entropy alloys.

2.1. Motivation

The need to supply global energy demands, requires new methods of energy production. These methods must yield enough energy and at the same time consider the greenness, to prevent global warming and limit CO_2 emissions to the legislated levels.

One of the methods pursued is the production of electricity through fusion reactions. The future achievement is a joined effort between multiple fields of science and engineering. Physics, plasma, mechanics, logistics, energy, electronics and materials. The need for better materials that can withstand the new challenges promoted by the need of modern technologies. The most well-known project is the multinational collaboration of the International Thermonuclear Reactor (ITER), located in France.

The reactor is based on the tokamak magnetic confinement concept. A magnetic field interact with the plasma particles, confining it in the shape of a torus. This plasma reaches temperatures in the order of 100 000 000 K and releases neutron to the first wall with energies up to 14 MeV [1]. The reaction occurs in a vacuum and the walls of the reactor are covered by a “blanket” that heats up with the kinetic energy of the neutrons, this energy is collected by the coolant to then produce electricity. One of the critical parts is the divertor, this part has the function of removing helium ashes from the plasma that hinders its efficiency, minimizing contaminations. It is located at the bottom of the vacuum chambers and possesses three targets that are located at the crossing zones for the magnetic field, becoming areas of large irradiation and heat flow (up to 20MW/m^2) [2].

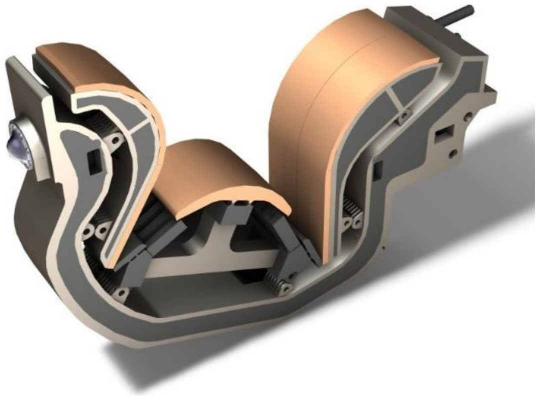

Figure 2-1 - Concept art of the ITER divertor [2]

A materials compatibility issue arises in the current divertor design. Tungsten with a melting point of 3685K, high sputtering threshold and low tritium inventory [1] [3] is the main candidate for the plasma facing material and CuCrZr, an alloy with high conductivity and strength [4], for the heat sink material. The issue arises in a dissimilarity between both materials: the high ductile-brittle transition temperature (DBTT) of tungsten, between 670 to 870K [5], demands higher working temperature, while CuCrZr possesses a low service temperature, up to 570K [6] due to oxidation and softening at higher temperatures, coupled with radiation embrittlement [7]. This will lead to a less efficient heat extraction and lower service life, and therefore a thermal insulation layer is necessary.

2.2. State of the art in thermal barriers interlayers

Between tungsten, the plasma facing material, and CuCrZr alloy, the heat sink, pure copper is currently used in the ITER. It is an interlayer that promotes easy joining and compliance [8] but no thermal insulation capabilities. Instead of a simple compliance layer, the use of the “thermal break” concept will improve materials interactions.

Multiple methodologies for interlayer thermal barrier technology are proposed. Interesting approaches such as the use of diamond-copper composites [9], however the high temperatures and neutrons interactions in the fusion reactor lead to the formation of a carbon phase between graphite and diamond [10]. Another approach used a composite material of W-monofilament reinforced Cu [11]. Unfortunately, thermal fatigue is noted due to the thermal mismatch between the tungsten wires and the copper matrix [12]. Functionally graded materials (FGM) [13]–[15] attempt to overcome the issues by having a material gradually change its properties from one interface to the other, to maximize the compatibility.

The lack of materials capable to fulfill this role drives the search for new better materials. A potential for this are a new realm of metallurgy, the high entropy alloys, described in the next section.

2.3. High Entropy Alloys

Current use of metallic alloys is limited to compositions based on a main element, with minor additions for tailoring properties, which also limits their advances. Examples are such as aluminum, titanium, nickel, magnesium and iron alloys. Some cases may take large additions of another element, like in bronze, brass alloys and stainless steels, but use of more than three elements in equiatomic compositions is limited. This leads to major knowledge on the edges of phase diagrams but limited to the more central regions with higher percentage of elements. High Entropy Alloys (HEA) represent a new realm of metallurgy in the sense that they are not based on a major element (solvent), but incorporate at least 5 elements, with compositions ranging from 5at% to 35at% [16]. Work on such concentrated systems has been limited, because of the prediction of the formation of a high number of phases by the Gibbs rule, the more elements exist in the system the more phases can be created.

Brian Cantor initiated his work in 1981 with his undergraduate student[17], publishing their results in master's thesis of following up students. They studied alloys with up to 20 components. However, these were multiphasic and brittle. From one of the formed phases of the samples, the CoCrFeMnNi composition was extracted, which lead to obtaining a 5 component equiatomic alloy with a single FCC solid solution. The work was only published for peer review in 2004 [18].

Jien Wei Yeh also began work with students, in 1995, posting their results on master thesis. In 2004 as well, his group published two papers on the subject [16] [19]. These articles revealed possible applications of such materials, thus propelling the field.

Ranganathan aided in the propelling of the field, not only by its contribution in its study, but also by sparkling interest with his talk on the alloying pleasures in metallurgy, where he referred this new topic, as well as other like gum metals and metallic glasses[20]. Full details of the story and origins of HEA can be found in the two books covering the field [21] [22], with participation from the pioneers.

Ever since their introduction by these pioneers the number of articles on the subject (Figure 2-2), rose together with the increasing interest of the scientific community. This arose from the fact that these alloys could be produced by common methods already applied in the current industry.

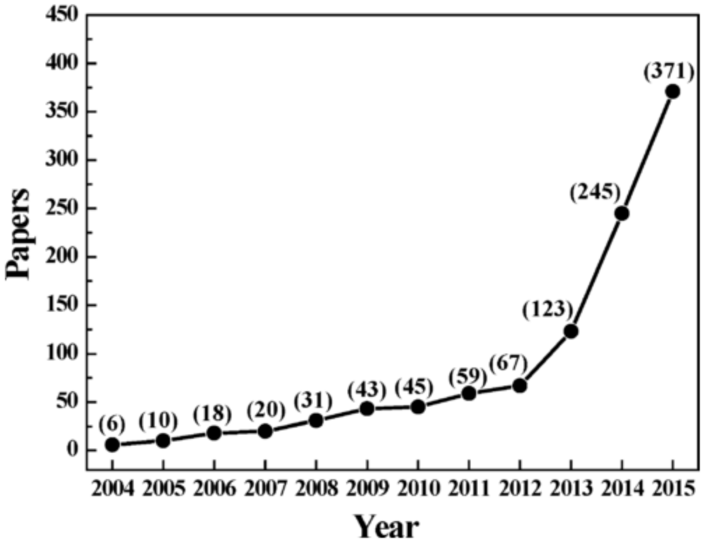

Figure 2-2. Rise of number of published papers per year on HEA [22]

2.3.1. Definition

High entropy alloys contain at least 5 elements or more, in equal proportion or with variations close to equiatomic. The term high entropy alloy was presented by Yeh [16], based on one of the effects proposed to stabilize the concentrated solid solution – the configurational entropy. Cantor also defined them as multi-component alloys [18], but other names such as multi-principal-elements alloys, equi-molar alloys, equi-atomic ratio alloys, substitutional alloys can also be used [23], [24].

The main concept used in HEA is entropy itself. Entropy is associated with the concept of randomness, or an attempt to quantify the randomness in a system, for instance in how many different ways can the energy be distributed through a certain number of particles in a system. The more random a system can be, the higher the entropy effect on such system. We can use statistical thermodynamics to quantitatively determine the randomness of a system following the Boltzmann hypothesis:

$$S = k\ \ln(\omega) \qquad (2\text{-}1)$$

Where k is the Boltzmann constant, 1.38× $10^{-23}\ J/K$ and ω is the measure of randomness in the system – how a system can distribute itself e.g. how thermal energy can be spread through a system. [25]

In the case of mixing various atomic species, ω will be simplified by representing configurational disorder, indicating all the diverse ways in which the different atoms composing the alloy can be distributed in a solution (in a random fashion). Entropy has contributions from configurational, vibrational, magnetic dipole, and electronic randomness. Although all contribute to the entropy, configurational entropy is dominant over the other three contributions [16]. Thus as an approximation for a liquid alloy or solid solution near the melting point containing n elements, we can quantify the configurational entropy change of ideal mixing per mole [25]:

$$\Delta S_{conf} = -R \sum_{i=1}^{n} X_i \, ln \, X_i \qquad (2\text{-}2)$$

Being *R* the gas constant 8.314 J/K mol, and X_i the molar fraction of the *i*-th element.

When considering an equiatomic alloy, we can use:

$$\Delta S_{conf} = R \ln(n) \qquad (2\text{-}3)$$

Where n is the number of species in the alloy.

Thus, we can obtain the following values, in the table, for the configurational entropy of alloys up to 13 elements.

Table 2-1. Variation of entropy with increase of elements in alloy

n	**1**	**2**	**3**	**4**	**5**	**6**	**7**	**8**	**9**	**10**	**11**	**12**	**13**
ΔS_{conf}	0	0.69R	1.1R	1.39R	1.61R	1.79R	1.95R	2.08R	2.2R	2.3R	2.4R	2.48R	2.56R

Taking the Gibbs free energy of a system:

$$\Delta Gmix = \Delta Hmix - T\Delta Smix \qquad (2\text{-}4)$$

Where ΔG_{mix} is the gibbs free energy of mixing, ΔH_{mix} is the enthalpy of mixing, T is the absolute temperature and ΔS_{mix} is the entropy of mixing.

Taking the alloy at the melting temperature, we know that at that instant the variation of Gibbs free energy is zero at equilibrium. Establishing $\Delta G_{mix} = 0$:

$$\Delta Smix = \frac{\Delta Hmix}{T} = \frac{\Delta H_f}{T_m} \qquad (2\text{-}5)$$

Where T_m is the melting temperature and ΔH_f the enthalpy of fusion. This entropy associated to the change from the liquid to the solid state is the entropy of fusion, and according to Richard's rule [26], the change of entropy from solid to liquid is a constant similar to *R.* Accordingly it is possible to estimate ΔH_f.

$$\Delta H_f \approx RT_m \qquad (2\text{-}6)$$

This means that if we increase the entropy of mixing to values around *R*, at high temperatures the alloy will be in good position to decrease the free energy of the system, competing with the enthalpy of formation of ordered compounds. Being that stoichiometric compounds do not possess configurational entropy due to their order, their contribution to lower free energy comes mainly from enthalpy change. At high temperatures this chemically ordered structures can be stabilized by vibrational entropy, but its contribution is still lower than the configurational one [27].

As a summary, high entropy alloys are alloys that rely on their high configurational entropy, more relevant at high temperatures, to compete with the high negative enthalpy of formation of ordered compounds. Upon their formation they can inhibit or alter the formation of these compounds [28], thus leading to the creation of simple structures with fewer phases than the predicted by the Gibbs phase rule. Being that these structures are disordered at the chemical level but structurally ordered, although no expected lattice site preference occurs for specific atoms, the structure is not amorphous and the overall atoms are arranged in a crystalline matter. For ordered phases, intermetallic or intermediate phases where elements have preferred positions in the lattice, this could be both stoichiometric compounds or ordered phases with a broad composition range, like Laves phases or intermetallic compounds.

Although as seen in Table 2-1, an equiatomic alloy with three components, already possesses a configurational entropy larger than *R*. However, in order to compete with compounds with very high enthalpy of formation like NiAl and TiAl, values around 1.5R are the lower limit [26]. Thus, it is established the minimum number of elements as five, with a change in configurational entropy of 1.61R, to promote solid solutions at high temperature.

An upper limit of 13 elements is established being that an increase in more elements will not yield much increase in configurational entropy and consequently no benefit to the high entropy effect.

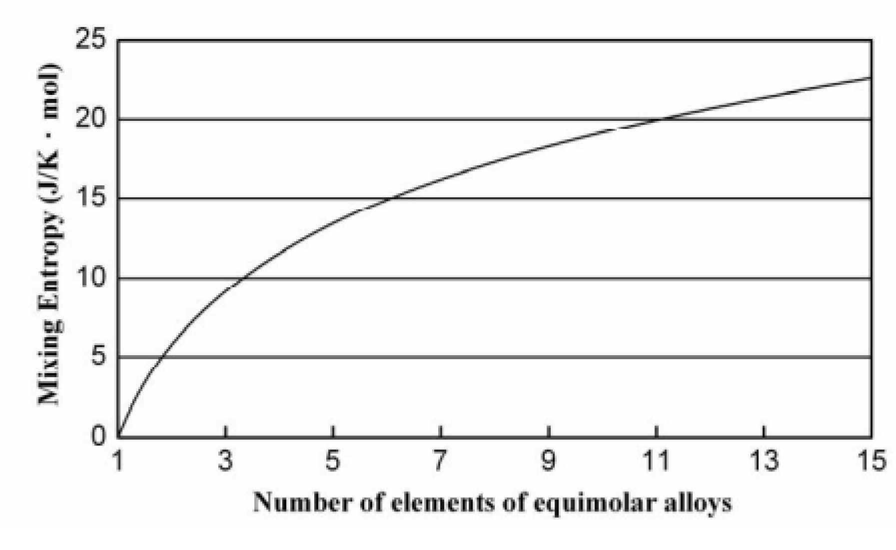

Figure 2-3. Variation of mixing entropy with number of elements in equimolar proportion [29]

Going from 13 to 14 elements the increase is only of 0.07R. As seen in Figure 2-3, the rate of increase in entropy reduces after the thirteenth element. The addition of further elements does not withdraw being named as an HEA[29] [26].

In terms of compositions, additions above 5 at.%. are considered main elements that contribute heavily to the entropy effect. Once again using the basis of 1.5R as the minimum configurational entropy, a mixture with a component with a concentration of 5 at.%, yields a contribution of 0.15R, only 10% of 1.5R. Any smaller addition will have lower contributions[26] and will be regarded as minor alloying additions.

This does not means that only disordered solid solutions are sought after, and as such does not exclude that tailoring of the formed phases, whether disordered or ordered can lead to improved properties [28].

2.3.2. Nomenclature

HEAs are not based on a solute-solvent basis, their compositions are not defined as specific elements alloys, with numbers and letters that mean alloying and/or treatments, like in aluminum alloys. The current nomenclature lies in identifying just their compositions and not any treatments. The notation has not been officially defined but is common to follow certain guidelines.

The name of the alloys is represented by its components in alphabetical order, the quantity of elements is defined by a subscript whether in atomic percentage or atomic ratio, equiatomic alloys can just have their elements ordered without any number added. For example, CrCuFeTiV represents an equiatomic alloy whereas $CrCu_{0.5}FeTiV$ is an alloy in which the copper atoms are 0.5 ratio of the other elements. Quantifying in atomic percentage we would have the same alloy denoted as: $Cr_{22.2}Cu_{11.1}Fe_{22.2}Ti_{22.2}V_{22.2}$. In studies pertaining variation of a single element in the composition, a subscript can be used to define the varying element, e.g. $CrCu_xFeTiV$ for (x= 0.1, 0.5 and 1), represents quickly the three compositions that are studied. This notation is specified in [21].

The following phase identification method will be adopted. When referring a solid solution, it will refer to a solid solution with no order and of simple cubic structure, specifying the type, either with BCC (body centered cubic), FCC (face centered cubic) or HCP (hexagonal close packed). When referring to ordered structures, it will mean any type of structure that has ordered lattices, possessing ordering reflection peaks in the X-ray diffractograms, whether it is an intermetallic, intermediate or ordered superlattice. To distinguish the type of ordered structure, it is referred by its Strukturbericht notation.

2.3.3. Properties and phase rules

As high entropy alloys are fairly different than conventional alloys, four core effects were defined to explain the microstructures and properties arising in HEAs. These are the high entropy effect: influencing thermodynamics of phase formation; severe lattice distortion: modifying properties; sluggish diffusion: affecting phase transformation kinetics and cocktail effects: giving rise to unexpected properties. These effects were first proposed in 2006 [29], based on available knowledge and were reviewed later this year [30].

2.3.3.1. Entropy effect

The number of phases in an alloy at constant pressure in equilibrium condition is given by Gibbs rule:

$$P = C + 1 - F \tag{2-7}$$

Where *P* is the number of phases, *C* the number of components and *F* the maximum number of degrees of freedom. For alloy mixtures of 5 elements at constant pressure, a maximum of 6 phases would be expected to be formed, the truth is that a lower number of phases are observed, and even monophasic structures can be created. As shown previously in “2.3.1 – Definition”, the entropy effect is what defines the name of HEA and is responsible for stabilizing this low number of phases. By consequence a number of compositions have been obtained that form materials with single [31], [32] or more [33], [34] solid solutions.

2.3.3.2. Severe lattice distortion

As the phases are composed of a multitude of elements in the same solution, the crystal structure is a matrix that will become distorted due to the various atomic sizes. There will be heavy lattice strain and the atoms have different atoms as neighbors, as represented in Figure 2-4. Moreover, other factors such as crystal structure, binding energy and electronic distribution affect the lattice distortion. However, the structure is not amorphous as the Bragg's law is still obeyed revealing a lattice parameter for this distorted structure.

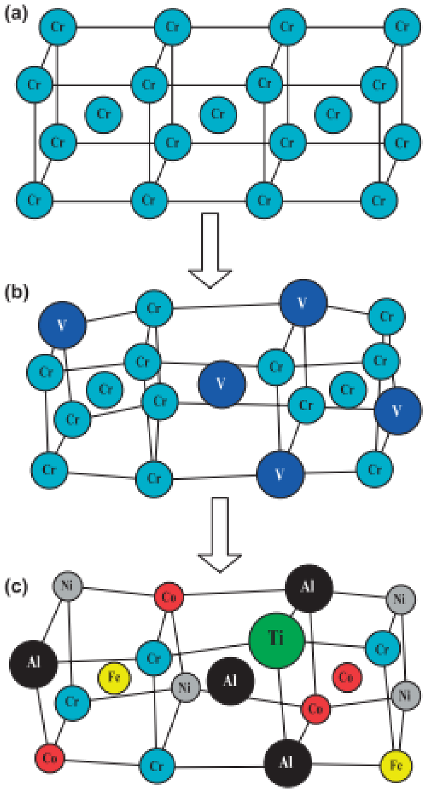

Figure 2-4 - Illustration of a distorted lattice, starting at (a) with regular solution of Cr and as more elements are added in (b) and (c) the lattices gets distorted due to the various atomic radius of the species [23]

The detection of diffracted X-ray reveals a reduction of intensity detection when compared with more diluted phases[36], like shown in Figure 2-4 a) and b). This effect is compared with the effect of the increase of temperature that reduces intensity of peaks, but it is verified that altogether this reduction of intensity is even more pronounced in HEAs. It would seem that the lattice distortion can then indeed reduce the intensity of the X-ray peaks.

This effect is one of the most relevant in HEA as it can induce great enhancement in properties, like increased hardness because of an increase in the solid solution hardening effect, by interaction of the dislocations with more strained lattice[37]. Changes in the phonon mean path by change in the lattice will lead to changes in thermal properties [38].

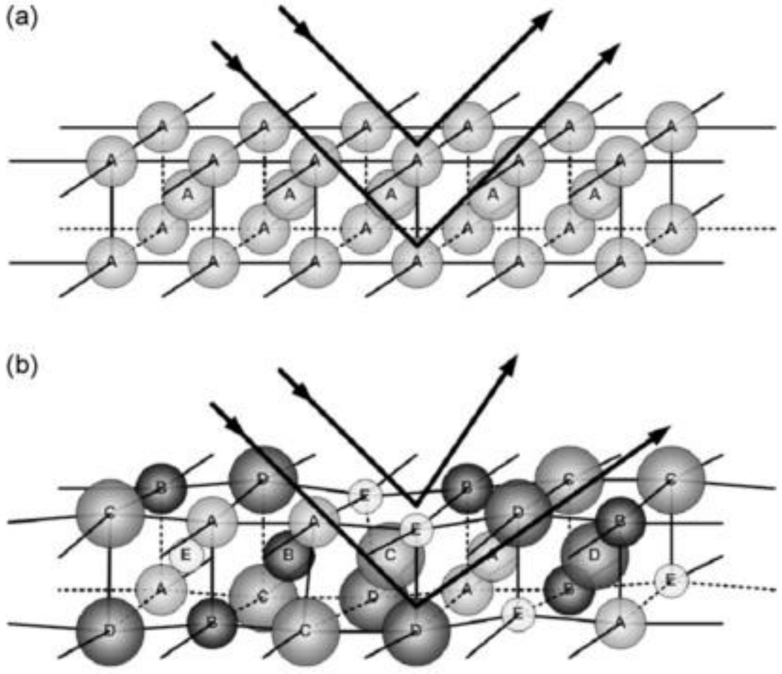

Figure 2-5 - (a) X-ray diffraction of solution of single component and (b) loss of coherence of diffracted rays in a multicomponent solution [36]

2.3.3.3. Sluggish diffusion

The diffusion at relative large distance of the atomic species controls the nucleation of new phases in, diffusion controlled phase transformations. The formation of new phases requires cooperative diffusion of various components. The vacancies are surrounded by different atoms that compete with each other, while at the same time the jump of a smaller atom to a vacancy site once occupied by a larger atom could lead to its entrapment while the opposite could even inhibit the jump of a larger jump altogether.

In concentrated alloys, is proposed that different atomic sizes and components can affect diffusion of the atomic species which has consequences on phase transformations and material properties. Experimentally this is observed in multiple cases, with benefits like the increases in recrystallization temperatures and reduced recrystallization rates [39], slower grain growth and particle coarsening during annealing, increases creep resistance [40] and phase stability at high temperatures in studies related to HEAs [41]. The effect gains support thanks to studies by Tsai et al. [42], with the use of diffusion couples that showed a higher activation energy.

The slower diffusion during phase formation is a property that would allow the stabilization of the solid solution at room temperature. When cooling a HEA from the liquid state, the free energy of the solid has a high contribution from the entropy thanks to the high temperatures at which it solidifies. However, as the solid cools this effect is reduced, but as the diffusion is sluggish the formation of ordered structure that are more stable at lower temperatures is slower [26]. This leads to the formation of fine precipitates or ordering of alloy that are very stable and can enhance the mechanical properties of the alloy. This is illustrated in Figure 2-6.

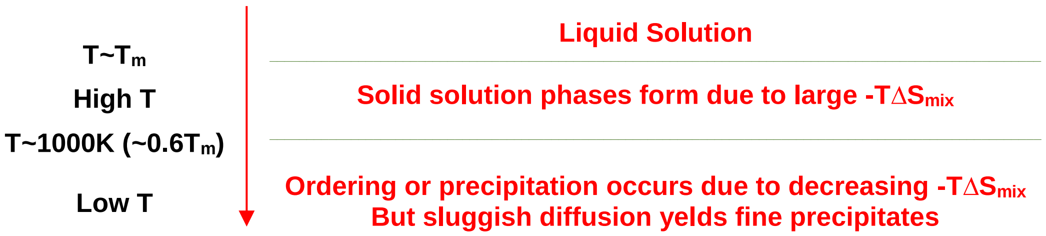

Figure 2-6 - Example of limit of ordered phase formation due to sluggish diffusion of an alloy with a melting temperature of 1700K [26]

2.3.3.4. Cocktail Effect

High entropy alloys are a mixture of multiple components, they can be seen as an atomic scale composite, in which each added element as a contribution to the “cocktail” as well as additional effects arising from specific interaction within this concentrated mixture.

A good example of this effect is the addition of aluminum to HEAs containing Cu, Co, Fe, Ni or Cr, which will promote a change in the stability of the crystal phase at room temperature [29] [43]. For an Al molar ratio below 0.5, the structure is FCC, as Al content increases the microstructure changes from a mixed FCC+BCC to a complete BCC structure. Alongside this transition an increase in hardness of the alloy is noted, likely associated with the inherent hardness of BCC structures in relation with FCC and also due to the high affinity of Al with the other constituent atoms. This transition has been attributed to the high lattice distortion induced by the larger Al atoms, promoting a less compact structure.

The development of refractory alloys with higher softening temperatures is achieved thanks to the cumulative effect of using high melting point elements, achieving superior performances when compared with Ni- and Co-based superalloys [32][44].

The design of the alloy $FeCoNi(AlSi)_{0.2}$ with high saturation magnetization, electrical resistivity, and malleability[45], was prepared by combining the ideal ratios of the ferromagnetic elements, Fe, Co and Ni, against the nonmagnetic elements Al and Si. The final “cocktail” giving the ideal properties.

2.3.3.5. Thermodynamics and empirical models

Even though there are plenty compositions that indeed form simple concentrated solid solutions, there are many others that don't. Whether they precipitate ordered compounds, or end in phase separation, this tells us that entropy is not enough to explain expansion of solid solubility limits of the alloys. Otto et al. [35] have effectively demonstrated this experimentally, a change in the microstructure was noted in an HEA that formed a single solid solution phase, when switching components but maintaining the configurational entropy.

Hume-Rothery (H-R) rules set a basis to predict solid solution formation in binary solid solutions. They are stated as:

1. The radii of the solute and solvent elements cannot differ by more than 15%. To obtain complete solubility, the atomic size difference should be less than 8%.

2. Crystalline structure should be the same to obtain extended solid solubility.

3. Same valency promotes extended solubility.

4. Similar electronegativity between elements prevent formation of intermetallic compunds.

When considering multicomponent alloys these rules can be expanded, as a basis to define empirical models to predict phase formation in HEA [30]. The used parameters are: the atomic size difference (δ), the enthalpy of mixture (ΔH_{mix}), the valence electron concentration (VEC), electronegativity ($\Delta\chi$). They are then brought together to establish how they affect phase formation rules in HEA. The basis for correlation are alloys produced from the liquid state due to the larger literature present on them.

The atomic size difference can be quantified as represented in equation (2-8) and (2-9) [46].

$$\delta = \sqrt{\sum_{i=1}^{n} c_i \left(1 - \frac{r_i}{\bar{r}}\right)^2} \tag{2-8}$$

$$\bar{r} = \sum_{i=1}^{n} c_i r_i \tag{2-9}$$

The enthalpy of mixture of the alloy is taken based on the binary enthalpy obtained by the Miedema model as noted in equation (2-10) [46].

$$\Delta H_{mix} = \sum_{i=1, i\neq j}^{n} 4 H_{ij} c_i c_j \tag{2-10}$$

With ΔH_{ij} the enthalpy of mixture of the binary pair *ij* calculated by the Miedema model.

These parameters are then compared directly with the experimental results from the studies of all the alloys. A criterion for establishing whether an HEA produced by arc melting would have tendency to form solid solutions, ordered phases or amorphous phase was demonstrated. For the atomic size difference values of $\delta < 0.066$ will have tendency to form solid solutions, while larger values will lead to amorphous structures. The ΔH_{mix} factor reveals that values between -11.6 kJ/mol and 3.2 kJ/mol are ideal for solid solution (SS) phases and more negative values promote amorphous phases. These two types of phases do not necessarily exist alone, there is a range for which ordered phases coexist with either solid solutions or amorphous phases.

Guo et al. [47] prepared a graphical representation combining these two parameters. In Figure 2-7 are represented the ranges for both δ and ΔH_{mix} that promote solid solution, amorphous phase or/and ordered phases. With δ a topological parameter is created in which it is noted that by increasing the difference in atomic sizes the structure gets further from forming a solid solution, this is attributed to a limit that a lattice can be strained until it collapses either to an amorphous phase or separates to form ordered phases [48]. With ΔH_{mix} a chemical parameter is introduced, solid solutions are then favored by values close to neutrality, meaning that overall there are little preferred pairs. However, as this value becomes more negative, intermetallic phase formation begins to overcome and even reaching the amorphous state, as the more specific the bonding is, the harder it becomes for the structure to form the desired crystal during cooling, forming an amorphous phase rather than a crystal.

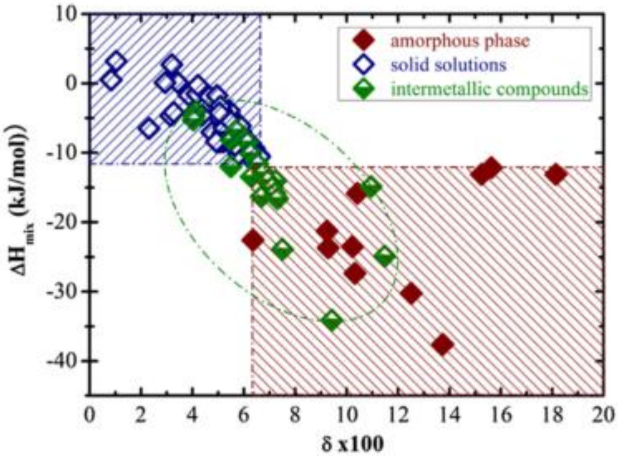

Figure 2-7 - Guo et al. δ - ΔH_{mix} plot representing phase formation rules for HEA. The blue regions denote solid solution, the red amorphous phase and the overlapping region represents the possibility of coexisting ordered phases with either SS or amorphous phase.[47]

In this previous model there is large uncertainty on the range of ordered phase formation. Yang et al. [49] attempted to shed some light on this and draw a more clear line between intermetallics and solid solution phase formation. For these the parameter Ω is used, described in equation (2-11), it consists of a ratio of the enthalpy contribution and the entropy contribution at the melting temperature. This method considers mainly phase formation at the melting temperature obtaining the maximum effect of entropy, ignoring solid state transformation at lower temperatures less relevant to HEAs, taking an estimated value of melting point from the law of mixtures in equation

(2-12). The higher the value of Ω the higher effect of entropy and more likely the formation of disordered solid solutions.

$$\Omega = \frac{T_m \Delta S_{mix}}{|\Delta H_{mix}|} \tag{2-11}$$

$$T_m = \sum_{i=1}^{n} c_i (T_m)_i \tag{2-12}$$

In Figure 2-8 the new established ranges of phase formation are depicted. The atomic size criteria remains unchanged as in the previous model. The new Ω parameter, reveals that the solid solution + ordered phase region is a transition to the formation of pure ordered structures. The solid solutions as expected are formed for Ω values larger than one and the amorphous structures arise from larger enthalpy contributions with Ω values lower than unity.

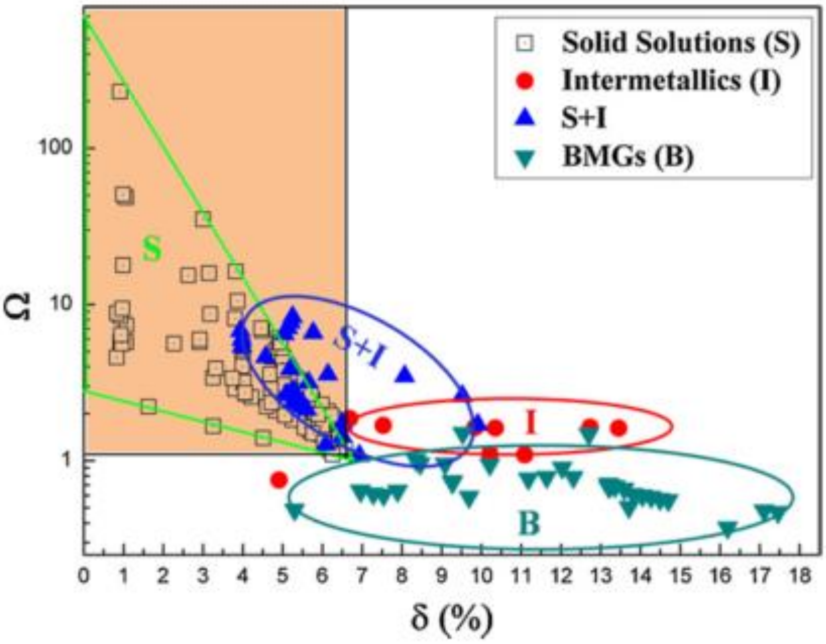

Figure 2-8 - Graphical representation of the Ω - δ parameters. A clearer separation between the solid solution stability region and ordered phases is noted[49]

However, these studies only consider the alloys in the as-cast state. Studies with the same systems upon annealing and homogenization reveal that the pure solid solution region is further shortened [50].

Pauling electronegativity of the alloy ($\Delta\chi$) is calculated as represented in equations (2-13)and (2-14).

$$\Delta\chi = \sqrt{\sum_{i=1}^{n} c_i (1 - \frac{\chi_i}{\bar{\chi}})^2} \tag{2-13}$$

$$\bar{\chi} = \sum_{i=1}^{n} c_i \chi_i \tag{2-14}$$

The valence electron concentration are the electrons present in the valence band of the atoms, other relations can be stablished such as the e/a, electron to atom ratio, but e/a values for transition metals are not very well defined[51].

$$VEC = \sum_{i=1}^{n} c_i VEC_i \tag{2-15}$$

No influence of Pauling electronegativity and VEC has been correlated to phase formation rules in HEA [51]. Although, the VEC parameter as shown that if a solid solution does indeed form with a simple cubic structure, VEC values larger than 8 will stabilize FCC structures, whereas lower values, VEC < 6.87, would stabilize BCC [51]. No studies proving this effect has been done for alloys produced with solid state methods.

2.3.4. Application of models and parameters

Relevant information regarding the elements used in the study is presented in the following tables. Information pertaining the elements individually is detailed in Table 2-2. In Table 2-3 the mixing enthalpy of binary pairs is presented.

Table 2-2 - Relevant information of elements and their allotropes used in the alloys

Element	Structure [52]	Lattice Parameter (nm) [52]	T_m /ºC [53]	Atomic Radius (nm) [54]	Atomic number[54]	VEC[55]	χ[55]
Cu	FCC	0.36146	1084.87	0.1278	29	11	1.90
Cr	BCC	0.28842	1863	0.12491	24	6	1.66
Fe-α	BCC	0.28665	1538	0.12412	26	8	1.83
Fe-γ[a]	FCC	0.36467	912[b] [56]				
Mo	BCC	0.31470	2623	0.13626	42	6	2.16
Ti-α	HC	a=0.29506 c=0.46835	1670	0.14615	22	4	1.54
Ti-β[a]	BCC	0.33065	882.5[b] [57]				
V	BCC	0.30240	1910	0.1316	23	5	1.63

[a] Allotropic form

[b] Temperature of allotropic transformation

Table 2-3 - Binary enthalpy of mixing ΔH_{mix} (kJ/mol) calculated through the Miedema model

Cu-Cr	12	Cr-Fe	-1	Fe-Ti	-17	Ti-Mo	-4
Cu-Fe	13	Cr-Ti	-7	Fe-Mo	-2	Ti-V	-2
Cu-Ti	-9	Cr-Mo	0	Fe-V	-7		
Cu-Mo	19	Cr-V	-2				
Cu-V	5						

Certain models designed to predict phase formation rules can be applied to our alloys, as described in the introduction of HEA. The values on which the models are based are present in Table 2-4. When applying the Boltzmann equation to compositional variation of our alloy system, we obtain as seen in the table the entropy variation. As already noted, configurational entropy attains a maximum value for the equiatomic composition.

Table 2-4 - Thermodynamic properties of the prepared HEAs

Composition	ΔS_{conf}	ΔH_{mix} **(kJ/mol)**	**δ (x100)**	**VEC**	$\Delta\chi$
$Cu_{0.21}CrFeMoTi$	1.52R	-5.33	6.71	6.25	0.23
$Cu_{0.44}CrFeMoTi$	1.57R	-3.13	6.59	6.5	0.22
CuCrFeMoTi	1.61R	0.64	6.33	7	0.21
$Cu_{0.21}CrFeTiV$	1.52R	-7.13	6.58	6.01	0.11
$Cu_{0.44}CrFeTiV$	1.57R	-5.4	6.45	6.28	0.12
CuCrFeTiV	1.61R	-2.4	6.15	6.80	0.13

Using the parameters of enthalpy of mixture and the atom size mismatch, we can compare what are the expected types of phase to form solid solutions, intermetallics, amorphous or a mixture of these, according with S. Guo et al. model [47]. According with the model solid solutions form with δ (x100) below 6.5 and with ΔH_{mix} values between -11.6 kJ/mol and 3.2 kJ/mol. Figure 2-9 is a recreation of the regions delineated by in Guo et al's work, with our systems added. Based on the

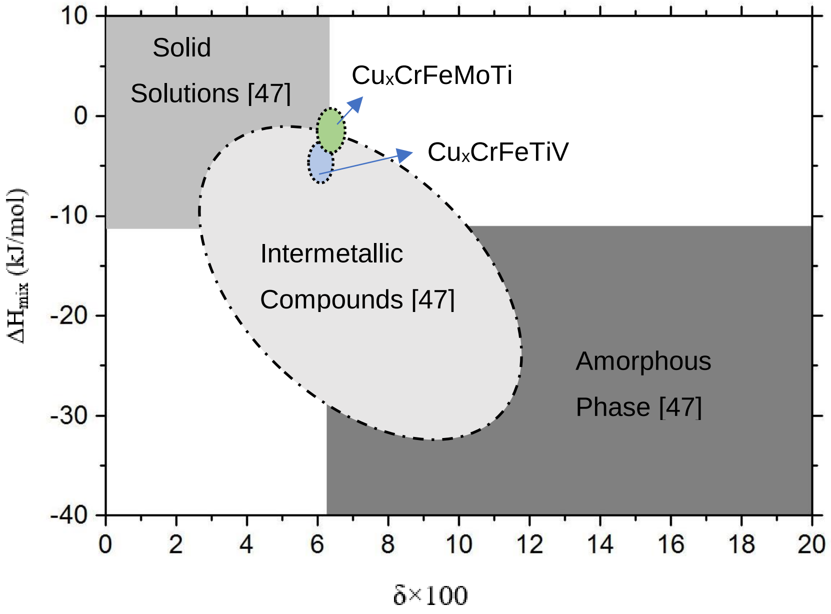

Figure 2-9 - Empirical relation between δ, ΔHmix, phase selection [47] *and the values for these systems* figure we expect the system to either form a mixture of solid solution with intermetallics, or one of either.

2.3.5. Production Techniques

High entropy alloys can be produced with conventional methods applied in regular alloys. Figure 2-10 reveals a summary of methods already used to produce these alloys. Samples can be produced in either bulk form or as film coatings. Depending on the processing methods different properties can be obtained meaning that choice of an adequate processing method will yield adequate properties.

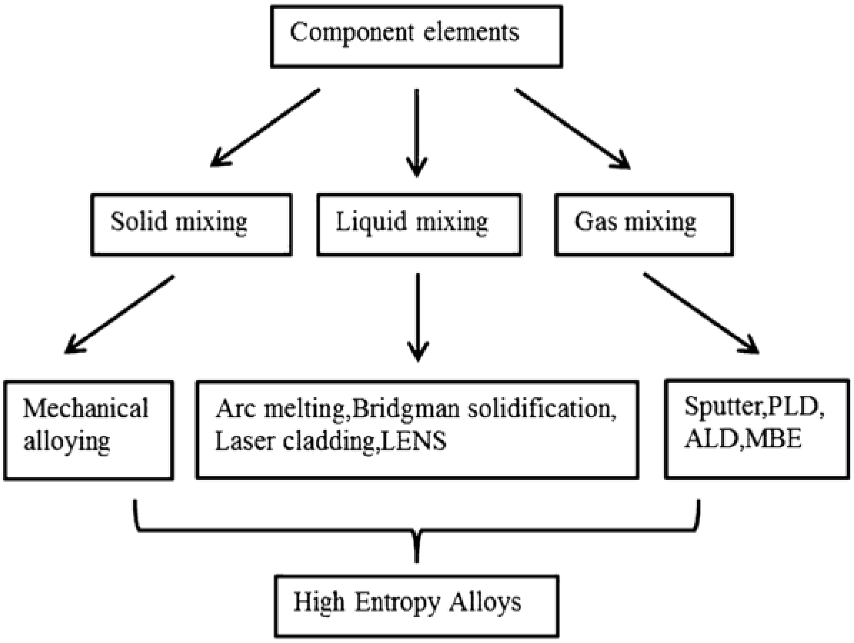

Figure 2-10 - Resume of production methods applied in HEA[22]

Liquid

Arc melting is the most commonly used method of production to study HEAs. The variety of metals that compose a high entropy alloy can be of very different melting points (as seen in [58] where an AlCoFeMoNiTi alloy containing Al that melts at 660ºC is mixed with Mo that melts at 2623ºC. As arc melting can reach very high temperatures, the full melting and mixture of all elements in the mixture can be guaranteed. The previously seen empirical models for phase formation rules, were based on the large list of samples produced through AM that exist in the literature [55]. Disadvantages arise as lower boiling point elements can evaporate, reducing compositional control [59]. Moreover, the as-cast structures can show chemical heterogeneities, by segregation or clustering of elements regions when working with atomic pairs with either high enthalpy of mixing [60][61] and phase separation due to the very different melting points of the used elements [62][44] during cooling. Physical inhomogeneity may arise by non-uniform distribution of dendrites forming regions of columnar grains and equiaxed regions [63]. As such, arc melting is an excellent method to obtain quick results of the phases that an HEA may give rise to, but in order to advance for large scale applications it must be aided by further processing. Homogenization of the as-cast structure, feasibility of texture control through cold-rolling and study of the stability of the metastable phases themselves [59][64]. Besides, Singh et al. [65] have shown how going from the liquid to the solid, the cooling rate influences the microstructure, which gives rise to the discussion of whether HEA metastable solid solution formation is promoted kinetically.

Solid state

The use of a solid-state route aims to prevent inhomogeneity defects arising in the liquid methods by preparing powder mixtures and consolidating alloys without reaching liquid state. The process consists of mixing and promoting solid solution formation between all the elements at low temperatures using mechanical alloying (MA). The mechanisms of MA and how the solid solution is achieved is expanded in Section 3 – Techniques and Procedure. The models for prediction of phases in HEA are based on the liquid route method, but mechanical alloying makes use of plastic deformation to force alloying and formation of solid solutions. Since the mix is done at temperatures that are not high enough for the entropy effect to overcome enthalpy effect the formation of ordered structures can occur. However some discussion arises as some authors still use the regular models to predict phase formation in solid-state production [66].

First studies of HEAs produced by mechanical alloying were done by Varalakshmi et al.[67]. The amount of literature published on solid state production of HEA is much more reduced when compared with liquid routes, although it has been ever-growing through the years. The appearance of HEA gave rise to studies on the competition of elements during MA [68][67][69][70] by increasing one by one the elements to be mixed and noting the effects. As the ideal milling time depends on when we have achieved a homogenous mixture, dealing with this larger number of components will give rise to different conditions for steady-state.

These studies have revealed mainly the factors affecting alloying order and phase formation. It was shown that the main factor controlling alloying was the melting temperature followed by the crystal structure and mechanical properties. The higher the melting temperature the stronger the bonding, making it more difficult for the elements to mix in a single alloy, affecting the solid solubility. This relates closely with their self-diffusivity coefficients and activation energies, which can be used to differentiate similar melting point metals. The crystal structures influence heavily the mechanical properties of pure metals. Besides lower melting point metals trending for softness, for instance, copper with a FCC structure is much softer, leading to easier alloying by covering the other elements through plastic deformation. The mixing enthalpy can also affect the alloying, positive will lead to rejection (by non-preferred pairs). While a negative enthalpy would enhance the mixing, however it was observed that melting temperature has a bigger influence on the alloying capacity of the elements[68]. The more elements are there to be mixed, the longer the milling takes due to lowering of their diffusivities [67] and upon milling for long enough time amorphization of the structure will happen [70].

The MA process creates saturated alloys, but in order to obtain a structural useful material consolidation is needed. There have already been used methods such as cold pressing and sintering, VHP, HIP [71] and SPS. The latter method is the most commonly used due to its low consolidation time that avoids grain growth, consequence of exposing the milled nanocrystalline powder to long sintering times[72]. Phase transformations of milled powders may also be of concern, as their thermal stability depends on their constituents [73]. Details on the operation of SPS equipment and mechanism is discussed later in Section 3-Techniques and Procedures. The use of heat treatments after consolidation is common to reduce internal stresses formed after the process.

Gas methods

Used most commonly for film production and they can lead to higher cooling rates (orders of magnitude higher) and consequently less segregation. For instance, in the system where usually phase separation of copper is noted in arc melting methods, the use of sputter deposition reveals all elements homogenously distributed in the thin film.

2.3.6. Properties and HEA system

2.3.6.1. Thermal diffusivity

There are few studies related to the thermal diffusivity and conductivity in HEA. The effect of larger lattice distortion can overcome thermal effects, as the lattice expansion due to temperature variations can be negligible when compared with the original distorted lattice [38]. Moreover, the existence of multiple different components can affect phonon mean free path, reducing diffusivity of energy while giving great stability to the structure through a high temperature range [74].

2.3.6.2. Radiation

Few studies so far have been undertaken on the effect of irradiation on HEA [75]–[78]. In light of all the observed properties that would be of potential use in a nuclear reactor, high temperature strength and corrosion resistance. Thanks to the heavily strained lattices of solid solutions, good radiation resistance was proposed. Egami et al. [79] proposed a self-healing mechanism after collapse of crystal structure to amorphous due to increase of the energy of the crystal due to the defects introduced by irradiation in the multicomponent system. The recristallization would then follow in the quench step of knock-on, which would generate a structure with less defects. Xia et al. [75] have demonstrated high stability in the $Al_xCoCrFeNi$ system with stable phases and low swelling.

2.3.7. Future

Still much more resources must be invested in predicting phase formation and stability, developing new models and criticizing the current ones. At an academic level, plenty of studies are provided on specific properties and the nature of HEA. Moreover, to mature HEA for industrial use a lot of work is required. Next studies are focusing on enhancing production techniques, verifying feasibility of mass production, weldability and even 3D printing.

This whole novel area of study gives rise to an enormous amount of possible combination of alloys. Studies are often accompanied by CALPHAD simulations [80].

This does not means that only disordered solid solutions are sought after, and as such does not exclude that tailoring of the formed phases, whether disordered or ordered can lead to improved properties [28].

3. Techniques and procedures

This chapter will list and describe the techniques used and detail the experimental procedures

3.1. Production and processing techniques

In this work, two production methods were used to produce the HEAs samples. A liquid route – vacuum arc furnace and a solid route – mechanical alloying followed by spark plasma sintering. Samples suffered modifications using ion beam techniques and vacuum annealing.

3.1.1. Liquid Route - Arc Melting

This method is fairly used to prepare alloys through mixing in the liquid state. As it can reach very high temperatures, around 3000K, almost any metal can be molten. In scientific studies, with smaller furnaces the piece is melted and remelted to ensure homogenous distribution of the elements in the liquid. Large industrial furnaces make use of stirrers, whether physical with gas, or magnetic, to ensure homogeneity and allow a continuous process without stops for remelting. The laboratory equipment is a simple setup, a small chamber in vacuum or containing an inert gas to avoid oxidation and contamination, with a tungsten electrode at the top and a cold copper crucible at the bottom. In this crucible, the raw material, whether lumps, rods or powder, elemental or alloyed, is molten and cooled. In our case elemental powders were mixed. It is in this vacuum between the top electrode and the raw materials that an arc will be created. The kinetic energy of high speed electron striking the material will rapidly increase its temperature.

3.1.2. Solid Route – Milling and Sintering

The solid-state processing involves the steps of preparing the homogenous mixture by mechanical alloying. To obtain the dense material for the envisioned application, the powder must be sintered, in this case using spark plasma sintering.

3.1.2.1. High energy ball milling

In high energy ball milling, the collisions between hard balls, vial and the raw material is used to promote transformations in the material. It can be used to homogenize powder mixtures of dissimilar materials, refine grain sizes, induce transformation, produce amorphous structures or create supersaturated solid solutions, all by mechanical action at low temperatures. Thanks to this technique amorphous alloys [81], quasicrystals, dispersion strengthened and nanomaterials can be prepared.

In mechanical alloying (MA) powders of different metals or compounds are milled together and material transfer between the powders is necessary to attain a homogenous mixture.

The process starts by inserting the weighted powders, alongside the balls in an appropriate ball to powder ratio (BPR), and a process control agent, inside the vial. There are multiple types of high-energy ball milling equipment that allow mechanical alloying with different geometries[82]. The equipment used in this work was a planetary ball mill. In which cylindrical containers with the balls and powder, spin around a central axis while revolving around themselves. The vial moves on one direction but rotates to the other, making the centrifugal force act on opposite directions. This leads to the balls moving alongside the wall of the vial and fractioning and grinding the powder. The balls, as seen on Figure 3-1, lift off and collide against the inside of the walls, promoting impact and simultaneous interaction between balls and powder, powder with powder and powder debris.

During the milling, the particles will continuously suffer fracture, cold welding and deformation [83], this will promote an increase in defects like dislocations, vacancies and more grain boundaries. These defects are the main responsibles for increasing the diffusivity and promoting a concentrated homogenous powder mixture. As we are dealing with pure metals, interactions are of ductile-ductile nature, meaning that the particles at initial stages, easily adhere to each other and plastically deform and agglomerate leading to particle size increase. This adhesion is necessary to promote the alloying of the elements with one another, as they form a composite lamellar structure, increasing their surface contact area and reducing the distances required for diffusion (Figure 3-2 a) and b) [70] shows particles at early stages of MA). As deformation continues the work hardening of the agglomerated powder leads to its fracture reducing particle size and refining its shape. A steady state is reached when the balance between fracture and

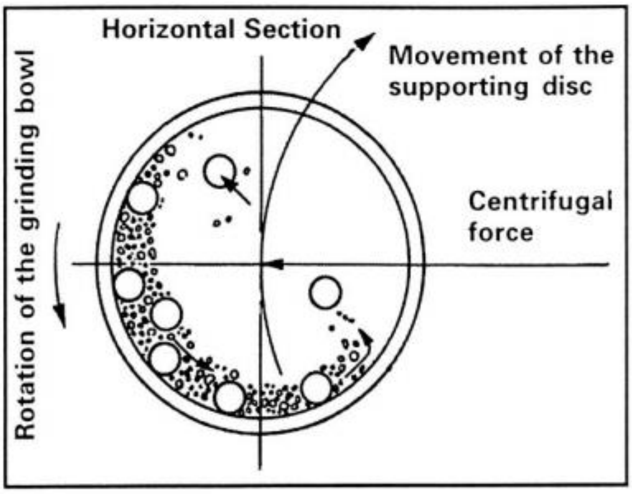

Figure 3-1 - Movement in a planetary ball mill [82] welding is even. It is this final homogenous powder mixture that will contain the HEA metastable solid solution.

A variety of process parameters can be controlled, and they will determine how the milling will occur. An exact comparison of the effects demands that the milling conditions are equal or very similar. Optimizing the conditions will lead to better results more efficiently, in less time. These parameters are not independent, they will affect the input of energy in the milled powders. Milling of powder in a regular atmosphere may lead to impurities in the mixture, such as formation of oxides.

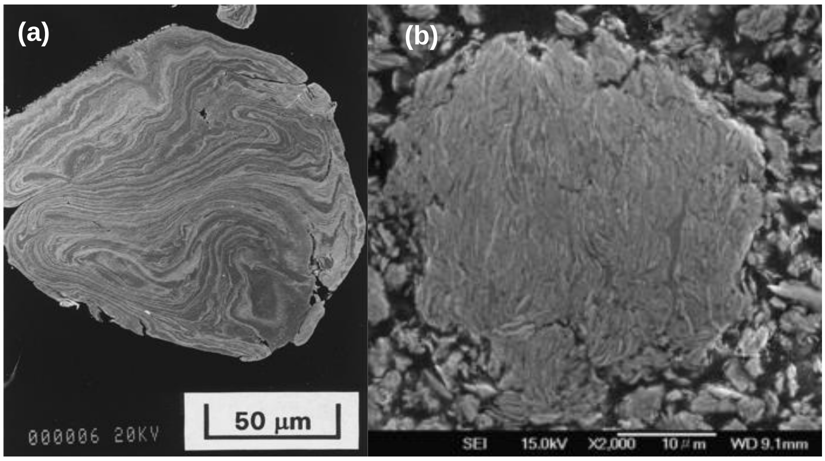

Figure 3-2 – (a) Lamellar structure that resulted from milling of silver and copper and (b) an octonary HEA [70]

The longer the milling time, the more homogenous the powder mixture is expected to be. Milling times should be kept to the minimum necessary in order to save energy and avoid powder contamination. The larger the ball to powder weight ratio, the higher the probability of collision and the more particles receive the energy from the mill. The relationship is exemplified in Figure 3-3. The speed of milling is defined as rotations per minute (RPM), faster values once again lead to faster homogenization but too much input of energy to the system can lead to temperature increase.

The Process Control Agent (PCA), is commonly an organic compound, at around 1 to 4 %wt of the mixture. It prevents large agglomeration of particles by reducing cold welding. The PCA also prevents the powder adhering too much to the surface of the balls, if there is a layer too thick around the ball, there is the risk of producing inhomogeneous powder, if it is too thin there may be contamination from the balls to the mixture. Excessive heating of particles upon collisions is also avoided thanks to PCA. This agent can lead to contamination of the powder during prolonged exposure.

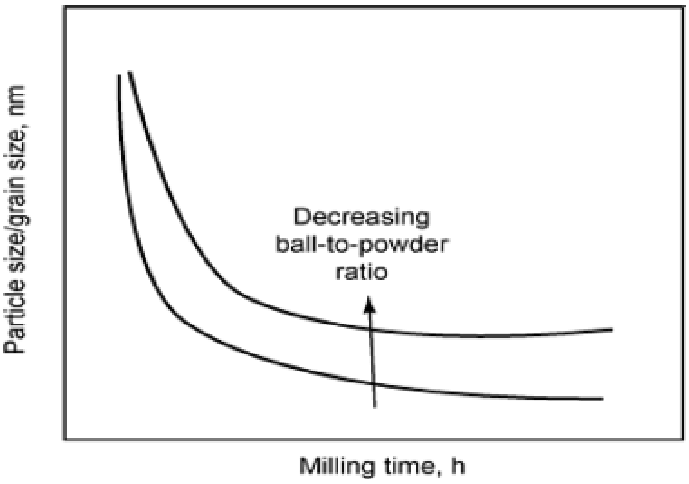

Figure 3-3 - Relation between decreasing particle size and milling time based on ball-to-powder ratio

3.1.2.2. Spark Plasma Sintering (SPS)

SPS is a sintering method used to consolidate materials in short time originating high quality low porosity sintered pieces. It can be applied to a multitude of materials: ceramics, metals, polymers and semiconductors. It can be used to produce materials that can't even be prepared without SPS like aluminum that cannot be sintered by conventional hot pressing processes[84].

The consolidation is characterized by the formation of plasma and electrical discharges that occur between the particles when applying pulsed current to the powder in a vacuum. When it comes to consolidation of metals, the consolidation is promoted by the localized elevated temperatures at the surface of the powders and discharges between them leading to increased mass transport. The process is proposed to have 4 steps [85]:

1) activation and refining of powders – spark discharges between particles remove impurities from their surfaces, such as oxides and contaminants;

2) formation and growth of sintering neck – the localized high temperature at the surface of the particles melts or even vaporizes the metal and creates necks by sputtering or diffusion to the next contacting particles;

3) rapid densification – the current passing through the so formed necks leads to joule heating which promotes diffusion;

4) plastic deformation densification – the application of pressure during the process together with the high heat softening of the boundaries leads to densification and elimination of any remaining porosity [86].

The bonding is enhanced by the cleaning of the particles by the activation step. As the temperature is raised locally on the surface of the particle, reaching 3000K [87], which is enough for most materials to melt and even vaporize leading to fast mass transport. Thermally the core is largely unaffected, thanks to this, amorphous structures can be maintained as well as nanograin dimension as the process does not give enough time or temperature for crystallization or grain growth. The short time, minutes rather than hours, and lack of grain growth gives advantages over other sintering methods like HIP [88].

Fast sintering is obtained from combination of spark discharge, joule heating and plastic deformation [88] and self-heating mechanism.

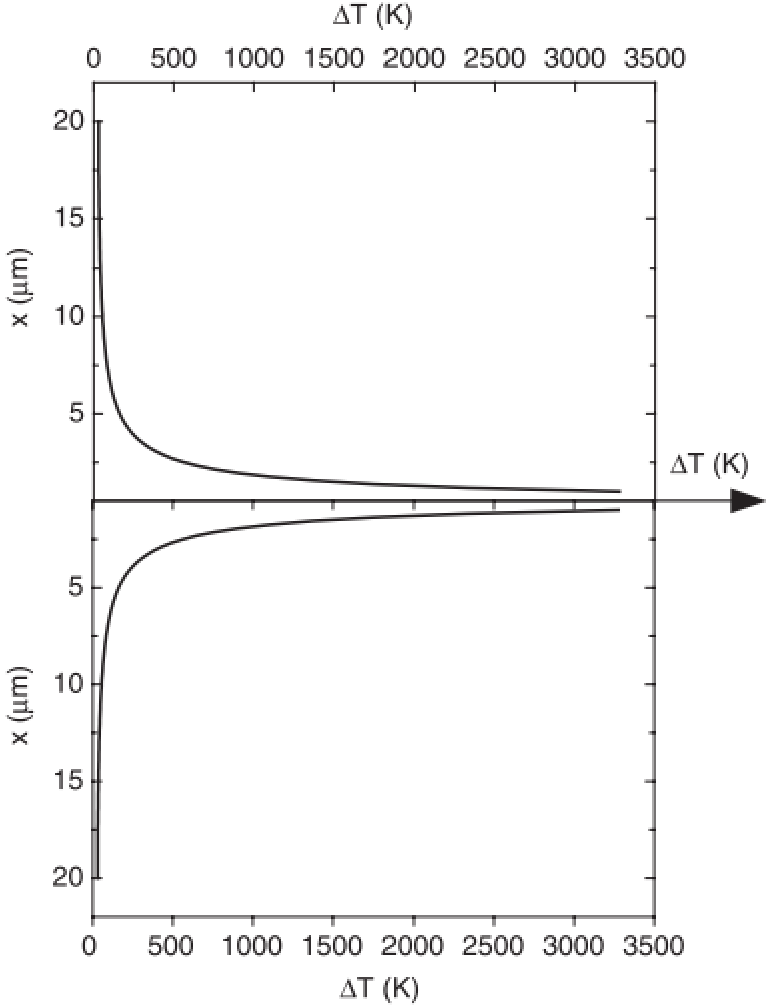

Figure 3-4 - Prediction of temperature variation from the contact point between two particles (x=0) to the interior of the particles (x=20) [87]

Usually the powder is placed in graphite dies, to which is applied initially a minimum pressure that can guarantee powder contact within the die. During the sintering the pressure is increased to the required value, being the maximum limited to the compression strength of graphite. Under vacuum, pulsed direct current is applied in the order of 2000 J for approximately 30 minutes, including heating and cooling cycle.

The hold time is usually in between 5 to 10 minutes, during which the maximum pressure and temperature are applied.

3.1.3. Ion Beam Irradiation

High energy particles can interact with matter leading to damage. The so-called radiation damage event arises as the energy from an incident particle is transferred to the solid matter, creating the primary knock-on atom (PKA), which moves from its original position and distributes the energy to surrounding atoms, this creates additional knock-on atoms. The damage event, occurs in a 10^{-11} s (10 ps) time frame creates a cascade of point defects and finishes with the PKA as an interstitial atom.

Radiation studies employs diverse types of particles: neutrons, electrons and ions (light or heavy). To study the effects of neutrons, energetic ions can be used. This technique gains traction as residual radioactivity is avoided as well as the use of the expensive test reactors. The replication of neutron effects with ion irradiation depends on the particle type and damage rate. Further incentive of ion beam methods, is the capability of providing answer while saving time and money when compared with neutron experiments. Ions allow variation of multiple parameters, such as dose, dose rate and temperature in a cost-effective way.

When comparing effects of energetic particles, the ideal factor to correlate results is the displacement per atom generated by the radiation. Dpa is calculated as:

$$dpa = \frac{Ndisplacements\ \times Fluence}{atomic\ density} \tag{3-1}$$

As represented by equation (3-1), dpa depends on the number of displacements promoted by the irradiating particles, the fluence that is the number of particles irradiated per unit of area, and the atomic density of the material.

Differences arise in depth penetration, while electrically neutral neutrons can penetrate millimeters of materials, ions will lose energy quickly via electronic interaction. Their penetration ranges only between 0.1 to 100 µm. Mass effect is also important, as light ions (electrons and protons) produce damage limited to Frenkel pairs or small clusters. Heavy ions and neutrons can promote damage in large clusters. These dense defects produced, end up recombining during cooling and quenching.

3.1.4. Characterization techniques

This section briefly refers the characterization techniques used in this work.

3.1.4.1. Scanning electron microscopy (SEM)

SEM is a technique that uses accelerated electrons at high voltages to obtain information about surface morphology, composition and crystal structures of a sample.

The type of generated image depends on the nature of the interaction of the electrons with the specimen. Secondary electrons (SE) are originated from the atoms in the surface of the sample: as the electron beam transfer energy to weakly bound electrons they are ejected from the atoms. These electrons reveal the topography of the surface as they give contrast to the image: darker regions corresponding to less detection of SE representing deeper areas. Backscattered electrons (BSE), are electrons that originate from the primary electron beam, but “bounced” back from the sample. The energy with which they return depends on the atomic mass of the containing elements, as such, the images obtained by BSE reveal elemental variations.

3.1.4.2. Energy dispersive spectroscopy (EDS)

Coupled with SEM is usual to have EDS equipment. When the accelerated electrons knock electrons from the inner shells, “holes” are created. These “holes” are then occupied by electrons from upper shell levels, releasing the excess energy as characteristic X-rays that can be used to identify and quantify the elements.

3.1.4.3. X-ray diffraction

X-ray diffraction makes use of the short periodical spacing between atomic planes in a crystal structure as a diffraction grating. Upon applying monochromatic X-ray radiation, X-rays specific angle of incidence in relation with the crystals will diffract obeying Bragg’s law of diffraction, originating an in-phase outgoing X-rays. These can be detected and distinguished from the background. The peaks originated by the diffractogram allows to determine crystal structure lattice parameters and spacing between lattice planes

For irradiated samples or for study of surface effects, grazing geometry can provide crystal structure information from the surface with less influence from the bulk material.

3.1.4.4. Electron backscatter diffraction

Electron backscatter diffraction (EBSD) also gives information on the crystal structure, but instead of X-ray photons uses the accelerated electrons from the SEM's primary beam. The sample is tilted in the vacuum chamber, and the diffracted electrons are detected on a phosphor screen, generating Kikuchi band lines. These patterns give information on the crystalline structure and orientation of the specific region where the electron beam is aimed. This allows to characterize crystal structure of specific phases and generate texture maps.

3.2. Experimental procedure

High entropy alloy samples of the $CrCu_xFeMoTi$ and $CrCu_xFeTiV$ systems were produced on a an atomic percentage basis and identified by their atomic ratio as suggested in the bibliography [21]. Six samples of two different systems were produced by a liquid route, vacuum arc melting, and one sample was produced via a powder metallurgy with mechanical alloying and consolidated by spark plasma sintering. Samples will be denoted by simply representing their composition and molar ratio for the samples produced by the liquid route, the sample produced through solid-state methods is denoted as CrCuFeTiV-MA.

3.2.1. Nominal Compositions

The following tables (Table 3-1 and Table 3-2) describe molar ratio and atomic percentages of the prepared compositions for the studied HEA systems,

Table 3-1- Molar ratio and atomic percentage of all the compositions of $CrCu_xFeMoTi$ system

Sample	Cu (at.%)	Cr (at.%)	Fe (at.%)	Mo (at.%)	Ti (at.%)
x=0.21	5	23.75	23.75	23.75	23.75
x=0.44	10	22.5	22.5	22.5	22.5
x=1	20	20	20	20	20

Table 3-2 - Molar ratio and atomic percentage of all the compositions of $CrCu_xFeTiV$ system

Sample	Cu (at.%)	Cr (at.%)	Fe (at.%)	Ti (at.%)	V (at.%)
x=0.21	5	23.75	23.75	23.75	23.75
x=0.44	10	22.5	22.5	22.5	22.5
x=1	20	20	20	20	20

3.2.2. Liquid Route – production

The starting material were small pieces, rods and lumps of Cr, Cu, Fe, Mo, Ti and V elements with purity >99 at.%, obtained from Alfa Aesar. The elements were weighed to obtain samples with compositions as described in Table 3-1 and Table 3-2. To increase the homogeneity a pellet with the correct proportion was prepared prior to melting. The alloys were melted in a vacuum arc furnace with a water cooled copper crucible, at least three times to ensure homogeneity before quenching to room temperature. The measured mass loss was less than 1%. Upon study of the $CrCu_xFeTiMo$ system a specific composition was selected for deeper study. The composition of the new sample, $CrCu_{0.17}FeMo_{0.17}Ti$, is fully defined in Table 3-3.

Table 3-3- Molar ratio and atomic percentage of $CrCu_{0.17}FeMo_{0.17}Ti$ system

Sample	Cu (at.%)	Cr (at.%)	Fe (at.%)	Mo (at.%)	Ti (at.%)
x=0.17	5	30	30	5	30

3.2.3. Solid Route - production

Through the solid route only one equiatomic sample (x=1) of the CrCuFeTiV system was prepared, the detailed composition is present in Table 3-2. This sample is the one denoted as CrCuFeTiV-MA.

Pure Cu, Fe, Cr, Ti and V metallic powders, with purities >99% acquired from Alfa Aesar, were blended in a glove box in an argon atmosphere. The powder suffered high-energy ball milling in a planetary ball mill, PM 400 MA Type, with stainless steel balls and vials. The ball to powder ratio was 10:1 (6.142g of powder to 63.260g of balls), and a solution of 90% ethanol anhydrous, 5% methanol and 5% isopropanol by weight, was used as PCA. The milling occurred for 40 hours (in cycles of 5 min on /5 min off) at 400 RPM, being that 20 hours were of effective milling.

The MA powders were consolidated by Spark Plasma Sintering, at a pressure of 65.2 MPa at 905/ºC with a holding time of 5 minutes. The process of heating and cooling took 25 minutes overall. Details of the pressure and temperature of the cycle are represented in Figure 3-5.

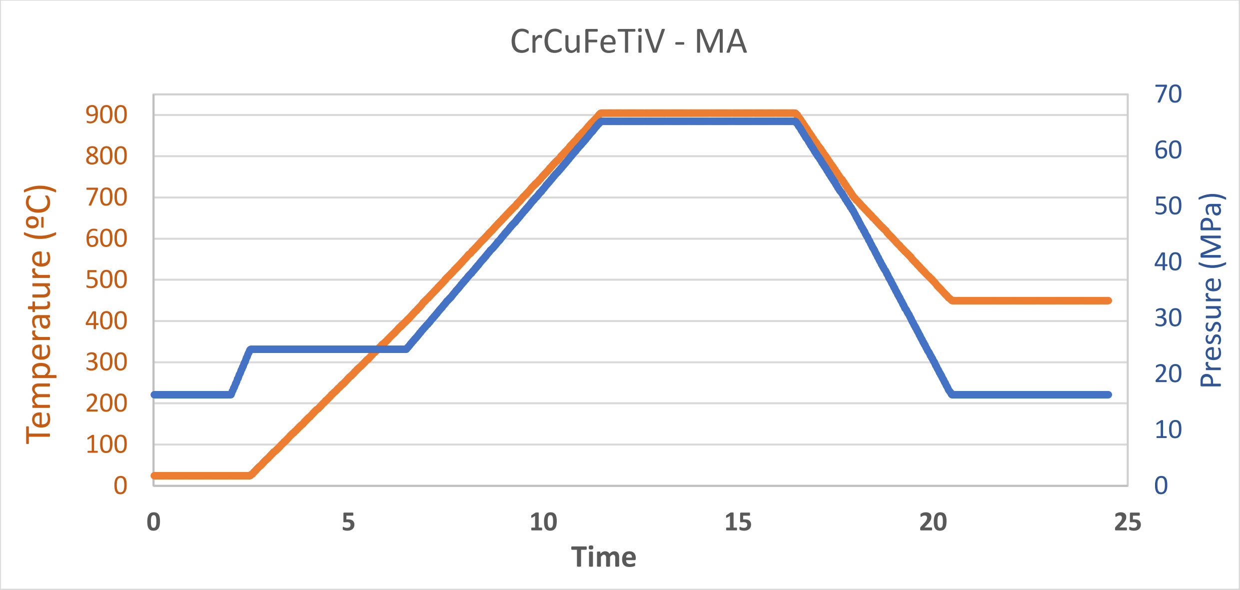

Figure 3-5 - Sintering curve showing variation of temperature and pressure with time

3.2.4. Irradiation

Irradiation was performed aiming to simulating in a few hours the equivalent effect of 5 years of continuous irradiation of neutrons in fusion reactors. According with Baluc et al. [1], damage rate in steels (dpa/year: displacements per atom per year) in first wall condition of fusion reactors, is of 20-30 dpa/year. This material in this study will work within the first wall, being a thermal barrier, meaning that it will not be submitted to as many neutrons as the first wall and will not have direct interactions with plasma and helium. It was then assumed a 20 dpa/year for the estimated operation time of a cassette divertor for 5 years, giving a total of 100 dpa throughout operation.

The equiatomic, sintered CrCuFeTiV-MA sample was submitted for irradiation. The irradiation energies and fluences used for the argon ions (Ar^+) were calculated using the SRIM software package [89][90]. To attain the peak damage of 100 dpa, 300 keV Ar^+ ions to the fluence of $3x10^{16}$ at/cm^2 at room temperature were used. The irradiated sample is denoted as CrCuFeTiV-imp.

3.2.5. Annealing

The irradiated sample, CrCuFeTiV-imp was annealed. The annealing was performed in a tube vacuum furnace at 800ºC for 1 hour, the vacuum level was $2x10^{-3}$ Pa.

3.2.6. Sample preparation

Metallographic preparation of the samples was performed by cold mounting specimens in epoxy resin followed by grinding with SiC paper and polishing with diamond suspensions (6 µm, 3 µm and 1 µm) and fine polished with oxide particle suspension (OPS).

3.2.7. SEM/EDS

The samples microstructures were studied with secondary electron (SE) and backscattered electrons (BSE) images with a JEOL JSM-7001F field emission gun scanning electron microscope equipped with an Oxford Instruments energy dispersive X-ray spectroscopy (EDS) system. To analyze irradiation damage, the sample was observed in SE mode and tilted 70º.

When performing elemental analysis accelerating voltage was at least 20 kV as per the thumb rule of applying energies 2 to 3 times higher [91] than the characteristic X-rays of the elements to detect.

3.2.8. X-ray diffraction

Powder X-ray Diffraction (PXRD) were collected at room temperature with monochromatic Cu Kα radiation using an Inel CPS 120 diffractometer. The samples were grinded to powder using a mortar. Samples CrCuFeTiV and CrCuFeTiV-MA where too hard to break in small parts and cryogenic grinding with liquid nitrogen in a tungsten carbide mortar was performed beforehand. The powder was placed on a silicon wafer and agglomerated with acetone. Analysis were performed in the 2θ range of 10º-80º, with 10 seconds scan and 2θ step of 0.04º.

Grazing Incidence X-ray Diffraction (GXRD) was performed on the sintered, CrCuFeTiV-MA and irradiated, CrCuFeTiV-imp samples with a Bruker D8 AXS diffractometer using the Cu $K_{\alpha1}$ and $K_{\alpha2}$ lines, and a Göbel mirror. The incidence angle with the surface was 2º, the step of 0.02º, with 60 seconds per measurement in the range of 2θ between 30º-100º.

The ICDD Database [93] was used for phase identification. The Powder Cell software package [94] was used to simulate diffractograms for comparison with experimental data and to refine the lattice parameters.

3.2.9. EBSD

For EBSD acquisition the samples were further polished with a 0.1 µm diamond suspension prior to etching with OPS. The sample was tilted 70º to acquire the EBSD pattern corresponding to the observed grain. Experimental patterns were acquired in three different grains of the same phas. Candidate crystal structures were selected based on results from the PXRD. The HKL Channel 5 software [95] was used for phase identification and index determination. The software calculates the reflected planes having significant intensity and automatically suggests solutions ranked by lowest mean angular deviation (MAD). MAD solutions under 1º were considered desirable for accurate solutions.

4. Liquid Route – Results and Discussion

This section will provide the results and the corresponding discussion of the experimental work for the samples produced by arc melting. Two systems were prepared via the liquid route using arc melt furnace, as described in Section 3-Techniques and Procedures. Casted samples will be named simply according with their composition: $CrCu_xFeMoTi$ and $CrCu_xFeTiV$, with the x varying depending on the molar ratio of copper composition. Phase identification will be in bold and use letters and numbers. The letter refers to the phase and the number to the sample, **1** being for the Mo and **2** for the V containing system.

4.1. $CrCu_xFeMoTi$

Three samples of the $CrCu_xFeMoTi$ system were produced by arc melting. The composition of the prepared samples was given in Table 3-1.

4.1.1. X-ray diffraction

The experimental diffractograms of the three compositions and the corresponding simulations are represented in Figure 4-1. Below the experimental results are adjusted simulated patterns to identify the experimental peaks. A hexagonal Laves phase (type C14) is present in all samples. Laves phase are compact structures of AB_2 type with a larger A atoms and smaller B atoms [96]. Another Laves structure is identified, the cubic Laves phase of type C15 is also present in all the samples. The CrCuFeMoTi is the only one that reveals the appearance of a BCC phase.

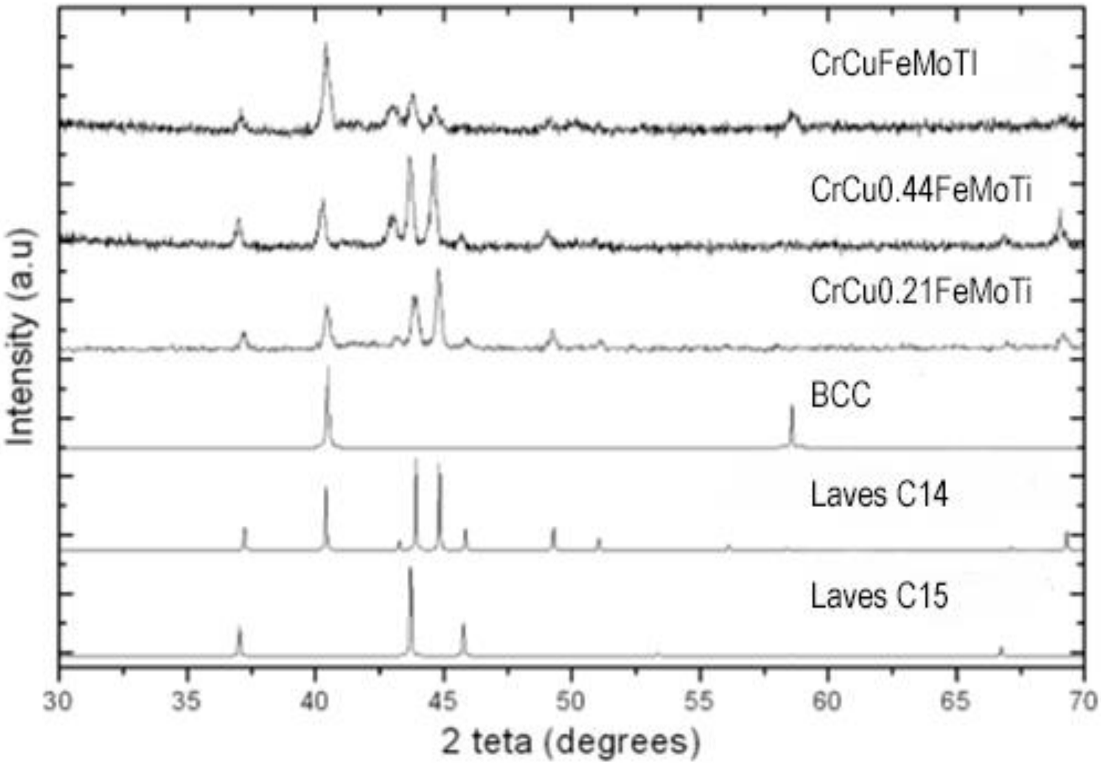

Figure 4-1 – Experimental diffractograms of samples CrCuxFeMoTi (x=0.21, 0.44 and 1) and simulated patterns.

The experimental lattices parameters of the indexed peaks, and the phase used as prototypes, are summarized in Table 4-1.

Table 4-1 - Identified structures and indexed lattice parameters of $CrCu_xFeMoTi$

Phase	**Pearson's number**[93]	**SGR**	**Prototype structure**	**Parameters (nm)**		
				x=0.21	**x=0.44**	**x=1**
BCC	cI2	Im-3m	W	-	-	a=0.31487
Laves C14	hP12	$P6_3/mmc$	$MgZn_2$	a=0.48265 c=0.78942	a=0.48437 c=0.79227	a=0.48445 c=0.789
Laves C15	cF24	Fd-3m	$MgCu_2$	a=0.68410	a=0.68653	a=0.68535

4.1.2. Microstructure analysis

Figure 4-2 presents the $CrCu_xFeMoTi$ system which revealed multiphasic samples and a microstructure evolution with increasing copper content.

There were 8 identified phases in total. Denoted as **A1**, the grey matrix region; **B1**, brighter regions mainly present at higher copper contents with defined edges; **C1**, is similar and appears next to **B1** but is less bright; **D1**, slightly dark regions; **E1**, the darkest regions, appears close to **D1**; **F1** and **G1** always appear tangles in one another, appears on the surface of **H1**, is slightly brighter than **B1** and their edges are smoother; and lastly **H1**, is the large brighter regions. Not all phases are observed in the same sample at the same time, phases **A1**, **D1**, **F1**, **G1** and **H1**, are the only ones common to the three samples. Going from the $CrCu_{0.21}FeMoTi$ to the $CrCu_{0.44}FeMoTi$ composition, phases **B1**, **C1** appear and phase **E1** disappears.

One of the main evolutions noted was that with the copper content increase of the samples, the volume fraction of dispersed phases, mainly phases **B1**, **C1**, **F1** and **G1**, through the matrix increase. Also, the change of the morphology of the dispersed phases, from roundish shapes in x=0.21 to directional growth in the other samples.

The elemental distribution throughout the phases in the sample was analyzed with EDS described in Table 4-2.

Table 4-2 - EDS results for phases observed in the CrCuxFeMoTi system. Phases F1 and G1 are not present because they form a very fine eutectic structure too small for a proper EDS analysis.

Phase	**Elements (at.%)**				
	Cu	**Cr**	**Fe**	**Mo**	**Ti**
A1	2.67±0.42	31.28±1.6	33.05±1.92	7.55±1.54	25.46±1.19
B1	88.45±0.16	1.91±0.13	2.50±0.04	0	7.15±0.02
C1	43.11±0.89	4.15±0.83	12.67±0.89	3.61±0.45	36.46±0.88
D1	9.89±2.67	14.52±0.43	24.83±1.13	1.4±0.52	49.37±2.05
E1	1.64±0.7	5.25±3.55	4.38±2.39	0	88.74±7.58
H1	0	0	0	100	0

CrCu$_{0.21}$FeMoTi

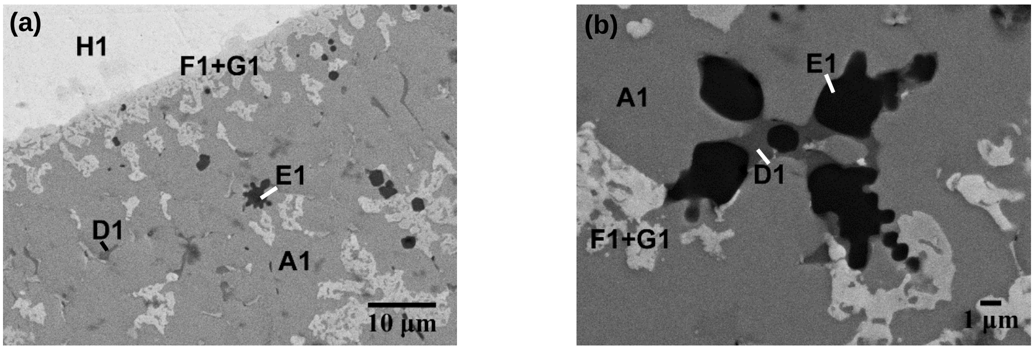

CrCu$_{0.44}$FeMoTi

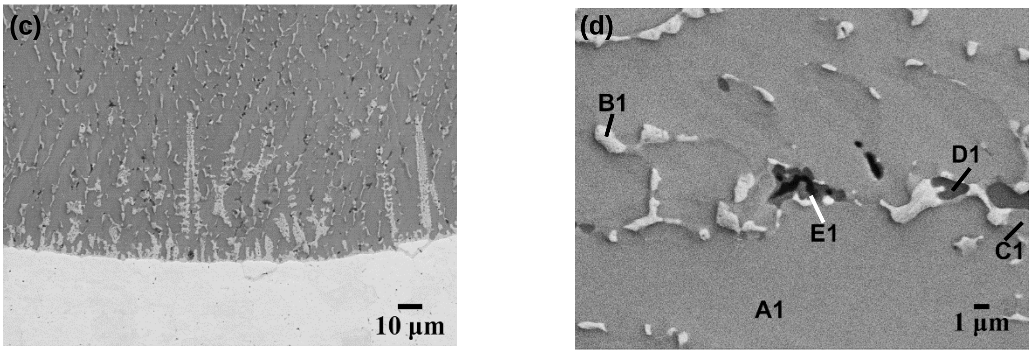

CrCuFeMoTi

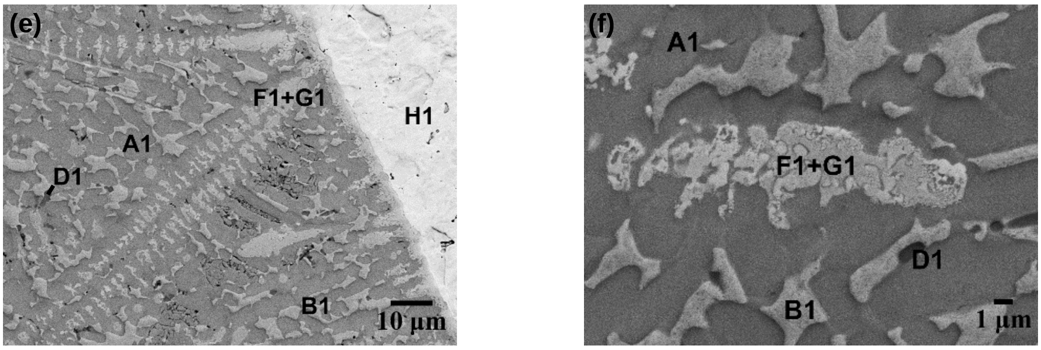

Figure 4-2 - Microstructures of CrCu$_x$FeMoTi for x=0.21 for (a) and (b); x=0.44 for (c) and (d) and x=1 for (e) and (f). As seen by SEM-BSE images.

4.1.2.1. Mo segregation

All samples revealed Mo segregation indicated as phase **H1** in Figure 4-2 (a), (b) and (c). This is supported by the bright backscattered electron regions, denoting the presence of the heavy elements, namely molybdenum the heaviest one in the alloy, together with an EDS result of 100% detection of Mo. In Figure 4-3, the low magnification images of $CrCu_{0.21}FeMoTi$ and $CrCu_{0.44}FeMoTi$, reveals large bright white region, denoted as phase **H1**, corresponding to segregated molybdenum. Since the raw materials for the samples were prepared from a pellet composed of small pieces (<0.5 mm), the formation of a single very large region of molybdenum indicates that Mo did indeed melt, and this phase originated from the liquid state. Furthermore, in the x=0.44 sample, the H phase possesses small regions containing dendrites, indicating the presence of liquid within the solidified Mo. Moreover, molybdenum rich grains revealed some pits which may have resulted from over-etching.

Looking at the evolution of the peaks of the XRD Figure 4-1, one may infer that the addition of copper leads to the stabilization of a BCC phase, as only the equiatomic sample reveals a BCC structure. Such fact is unexpected as the microstructures shows that addition of copper promotes the formation of copper rich structures. Besides, the nature of copper as an FCC promotor in HEA [97][98][99][100], would predict the appearance of FCC peaks. However, these BCC peaks that arise in the equiatomic sample, could be associated to the segregated molybdenum regions (phase **H1** in Figure 4-2), as the measured experimental lattice parameter is of 0.31487 nm, similar to the lattice parameter of Mo of 0.3147 nm [52].

This large segregation of Mo was the most unexpected phenomena, Figure 4-3. This could have been a result of non-equilibrium solidification of the alloys between the liquidus-solidus temperature range, making the distribution of elements in the growing solid kinetically restricted. This range is expanded by the difference of melting temperatures between the elements in the system[44]. Molybdenum, with the highest melting point of 2896 K [101] and the other alloying elements, specially copper, with the lowest temperature of 1358 K [101]. As noted in table 3-2 the enthalpy of mixing of Mo with most elements is close to zero but is very high in the case of copper, it is possible to infer then that Mo separation fron copper is favored.

So far, to our knowledge, there has been no other high entropy composition produced by arc melting that suffered such segregation, that depletes the rest of the microstructure of this element. In equimolar alloys composed of refractory elements, MoNbTaW/MoNbTaVW [44] [32] a single BCC phase is formed. Segregation is also observed, not to the scale seen in our sample, but as microsegregation, noted by the coring of the dendritic structure, the center being enriched by the higher melting point elements, $T_m(W) = 3695K$ vs $T_m(V) = 2193$ K.

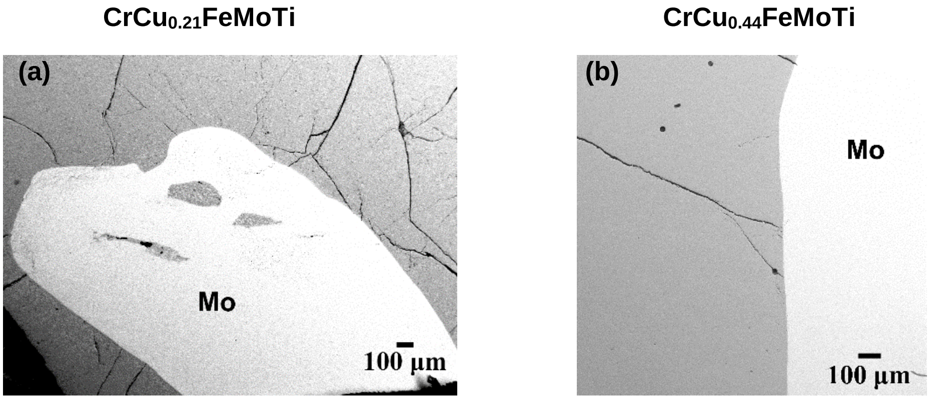

Figure 4-3 - Low magnification image of segregated Mo. (The white region represents Mo) for CrCu$_{0.21}$FeMoTi (a) and CrCu0.44FeMoTi (b).

A study on AlCrFeMo$_x$Ni (x=0, 0.2, 0.5, 0.8, 1.0) reveals solubility of the Mo atoms leading to great solid solution strengthening because of the lattice distortion, up to a certain percentage after which the lattice strain is to large, causing the appearance of a topological close packed σ phase that retains the excessive molybdenum[102]. A direct comparison is difficult to make because, although this system possesses a higher melting temperature difference, aluminum at 933K vs molybdenum at 2896 K [101], and even before the addition of molybdenum a phase separation had already occurred due to the formation of the ordered solid solution, based on the Al-Ni pair (because of the very low enthalpy of formation: -22 kJ/mol [103]).

Tsai et al. [104], have established a criterion to identify HEAs containing Cr and V that are prone to sigma phase formation, being those with VEC values between 6.88 and 7.84. From Table 2-4 it can be concluded that with this criteria only the composition CuCrFeMoTi is prone to its formation, but the study [104] did not refer to Mo containing alloys. It is possible to consider that perhaps the removal of Mo from the solidifying liquid could have prevented σ phase formation, as it is usual to find it Mo and Fe containing HEA [102][105][106]. The VEC for the compositions of the vanadium system fall outside the range for sigma stability, which supports the claims of Tsai et al. [104].

4.1.2.2. Fine eutectic

The samples also show the presence of what seems to be a fine eutectic (Figure 4-5) between phases **F1** and **G1** in the dendritic region. Due to the finesse of the structure no proper composition analysis was possible. However, the X-ray map exhibited in Figure 4-4 points to a Cr and Mo rich region and that the other phases are seen to not contain practically any molybdenum, making it clear that there was very low dissolution of Mo throughout the sample. The **F1** and **G1** are then the phases that dissolved the most Mo.

As the copper content increases **F1+G1** increases as well. The existence of a melt richer in copper could lead to forcing the formation of these structures, as Mo and Cu possess the highest enthalpy of mixture of the system, at 19 kJ/mol, their tendency is to repel each other. This is observed even in the sample with less copper, $CrCu_{0.21}FeMoTi$, in a region enclosed between a segregated patch of Mo, Figure 4-3. In the equimolar sample specifically, we note large dendrites of phase **F1**+**G1** crossing the matrix, Figure 4-2-e). In Figure 4-3 we note that for the sample with fraction of 0.21 copper, there is a region within the molybdenum grain that is surrounded with **F1**+**G1** phase. This eutectic is also noted at the surface of phase **H1**, noted in Figure 4-2 (a), (c) and (e), it could be that it is a preferred nucleation site for the two phases, it could be that this phase is formed through a peritectic reaction by consuming **H1**.

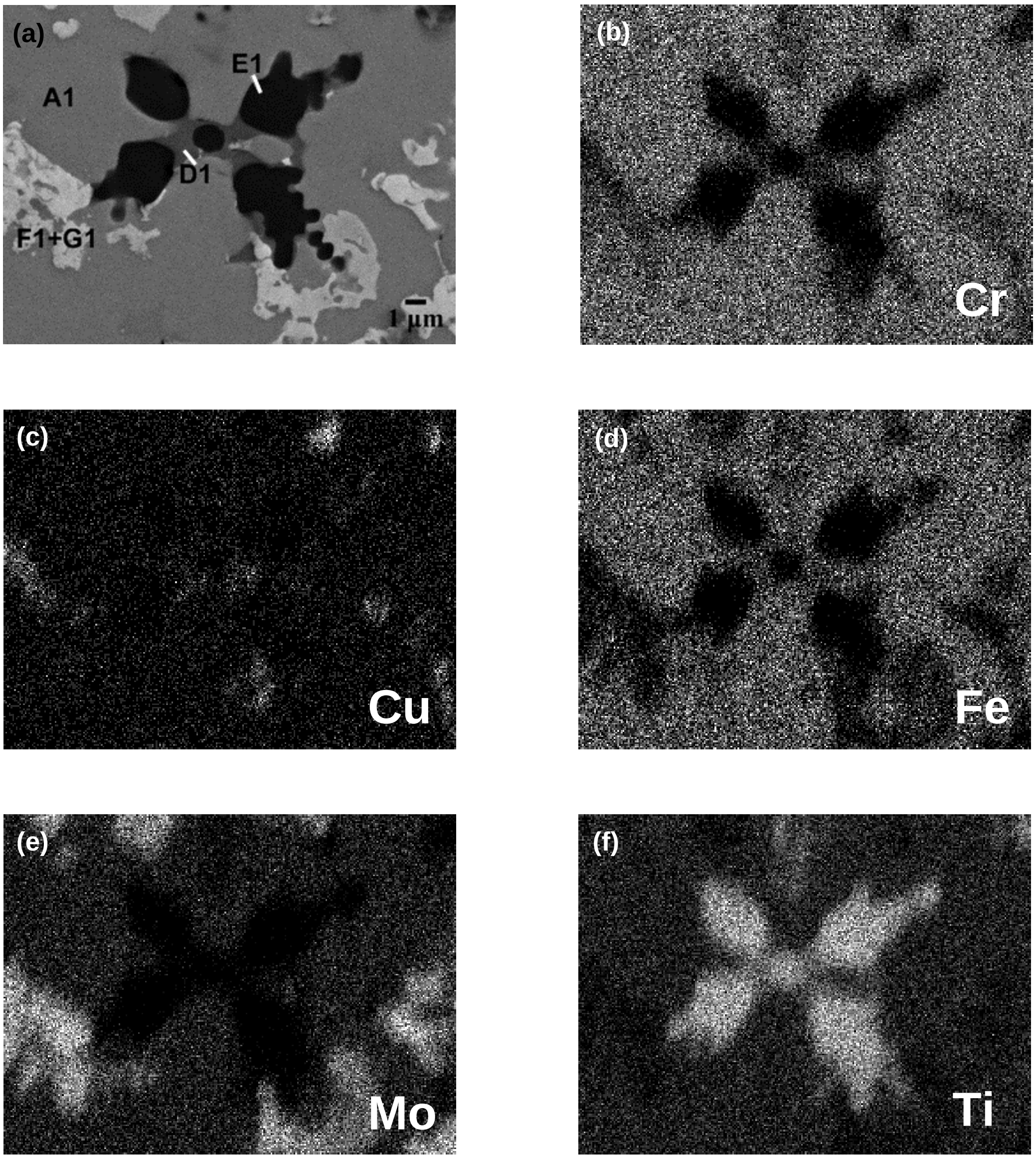

Figure 4-4 - (a) SEM/BSE image of the Cu0.21CrFeMoTi and the corresponding X-ray maps for (b) Cr, (c) Cu, (d) Fe, (e) Mo

Both chromium and molybdenum can be found together because of their zero enthalpy of mixture, same BCC crystal structure and similar electronic configuration[107] According to the binary Cr-Mo [108], both elements are soluble until at maximum 1150 K, where they form a miscibility gap.

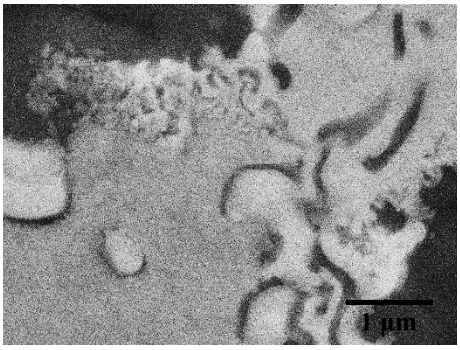

Figure 4-5 - Detailed view of eutectic in CrCuFeMoTi

4.1.2.3. Matrix phase

A majority phase, labeled as **A1**, rich in Cr, Fe and Ti, was observed in all microstructures, Figure 4-2. This structure reveals itself as a “matrix” phase that connects all the phases present. This phase’s volume becomes reduced as more copper is added leading to the appearance of more dispersed phases.

Preparation of HEA with a similar fraction of titanium as the other elements, in which these other elements are of smaller atomic size or/and in their binary phase diagram with Ti, will most likely lead to the formation of compact Laves phase [60], [99], [109], [110].

EDS (Table 4-2) evidences that close to a third of **A1**’s phase composition is titanium, and the rest is composed of mainly chromium and iron. Concerning the binary diagrams of the present elements, only the Fe-Ti and Cr-Ti pairs do form C14 type Laves phase. As such due to its composition and its presence of Laves C14, Figure 4-1, in all three samples it is suspected phase **A1** is an ordered Laves structure. This can be denoted as a $(Fe,Cr)_2Ti$ type phase, in which the titanium occupies the A sites and the other elements, being of the B type, occupy either B lattice sites or A lattice sites creating anti site-defects[111].

In terms of copper, the EDS reveals low quantity in the systems. Looking at the Cu-Fe-Ti [113] system, the C14 Laves phase shows very little solubility of copper, around 3% of copper can dissolve in this Laves phase at 850 ºC.

Both Mo and V are capable of substituting for Cr and Fe positions in the Laves phases. In the Fe-Mo-Ti ternary[114], the solubility of Mo in the C14 phase can be up to 25 at%. Perhaps more Mo would have been dissolved if it had not been lost by segregation.

The formation of such Laves phases and the information from the phase diagrams may indicate that in this system Ti may be one of the elements affecting simple solid solution formation. Considering the dimensional parameters, as Cr and Fe are similar in dimension but Ti is larger, this lattice strain would not be accommodated in a simple cubic structure, and for that we can see the formation of an ordered phase of lower entropy and with lower enthalpy because of the preferential pairs.

4.1.2.4. Dispersed phases

Phases **B1**, **C1**, **D1** and **E1** seem to nucleate together. We can separate these phases in two pairs. The first pair is **D1** and **E1** are titanium rich, **E1** having around 90 at% titanium and **D1** being around 50 at% Ti and 25 at% Fe. These two phases appear in larger volumes in the sample of lowest copper, x=0.21, Figure 4-2 (a) and (d). As the copper content increase we notice a shift from titanium rich phases (**D1** and **E1**) to copper rich phases: **B1** having close to 90 at% copper and **C1** around 43 at% copper to 36 at% titanium represent the second pair. Once again appearing next to each other, as seen in Figure 4-2, as for x=0.44 and x=1. The increase of copper leads then to the increase in size and number of copper rich dendritic structures. However, at the same time, the titanium rich structures do not completely disappear but appear at a smaller fraction associated with these copper rich phases.

The formation of Cu-rich regions like **B1** phase is commonly observed in HEA systems containing copper produced by arc melting. In fact, some of the most comprehensively studied systems contain copper, usually with elements like Al Co Cr Cu Fe and Ni [34], [39], [62], [65], [98]–[100], [115]–[117], mostly leading to FCC type structures, making copper an FCC stabilizer in HEA.

This tendency has been attributed to the positive enthalpy of mixture of copper with the other transition metal elements, table 3-2. For the elements in our studied system, copper only has negative enthalpy with titanium. Moreover, studies making use of Ab Initio Molecular Dynamics show that in the melt there may be short range ordering of some pairs that lead to clustering of copper, creating the observed multiphasic structures with copper rich regions during solidification [61], [80].

The mixing enthalpy effect gains traction with phase **C1**. These have between 45 % copper and 30% titanium most likely makes use of the low enthalpy of mixture between copper and titanium, -9 kJ/mol (table 3-2), to promote these preferential pairs. Both phases **B1** and **C1** appear together indicating their nucleation is dependent on one another. Using the Cu-Ti [118] phase diagram as a guideline, the compounds at a 30 at% of titanium possess a lower melting temperature than copper. It could be said then that the purer phase **B1** formed first, followed by the lower volume fraction phase **C1**.

The use of copper seems to be a large deterrent to reach single phase HEA. With a minor use of copper, possibly the separation of phases on cooling would be reduced. Increasing of the cooling rate may also be key on reducing phase separation. Singh et al. [65] have used splat quenching to produce copper containing HEA with less phase separation. Also change of the production method altogether, like using solid state processing (section 5 – Solid route).

Phase **D1** has around 50 % Ti and 25% Fe. The Fe-Ti pairs have the lowest mixing enthalpy of the systems at -17 kJ/mol (Table 2-3). Much like the previously discussed copper rich phase (**B1**), phase **E1** is titanium rich with 90 %at Ti. Both titanium phases **D1** and **E1** are observed, nucleating together and easily detected in the x=0.21 sample.

4.1.3. EBSD analysis

EBSD analysis was used to reveal the correspondence between the phases identified by SEM observation and the structures obtained by PXRD. It was performed on the surface of the three samples, and representative images are shown in Figure 4-6. The candidate structures were loaded into the Channel 5 software database[95]. Therefore, the identified structures were considered for EBSD simulations: two Laves phases, of $MgZn_2$ type with a hexagonal structure, of $MgCu_2$ type with a cubic symmetry, and a body-centered cubic structure of similar to Mo. Details of the space groups of the structures are given in Table 4-1)

The results indicated that the majority phase, regions **A1**, can be indeed indexed to the Laves phase of type C14, Figure 4-6 (c) and (d). Region **H1** revealed a correspondence to the simple cubic structure of molybdenum, confirming the origin of the BCC peak. Although this phase **H1** is present in every sample, the lack of the BCC peaks in both sample $CrCu_{0.21}FeMoTi$ and $CrCu_{0.44}FeMoTi$ is most likely consequence of using powder from a section of the sample, that did not contain this concentrated molybdenum, for the XRD.

Moreover, region **B1**, which is a Cu-rich phase, can be indexed to the cubic Laves phase of type $MgCu_2$ as well as to a BCC structure of Mo-type structure. For the $MgCu_2$ type Laves phase simulation pattern, the experimental bands seem to match with the simulation (Figure 4-6 (f)) and no bands are absent. However, the EDS results, in Table 4-2, reveals phase **B1** as a Cu-rich phase without the 1:3 ratio between large and small atoms typical of Laves phases, which may indicate that probably the structure is not exactly like the $MgCu_2$-type. When looking at the simulated BCC structure of Mo-type and the experimental pattern revealed that there are some experimental bands that are not indexed

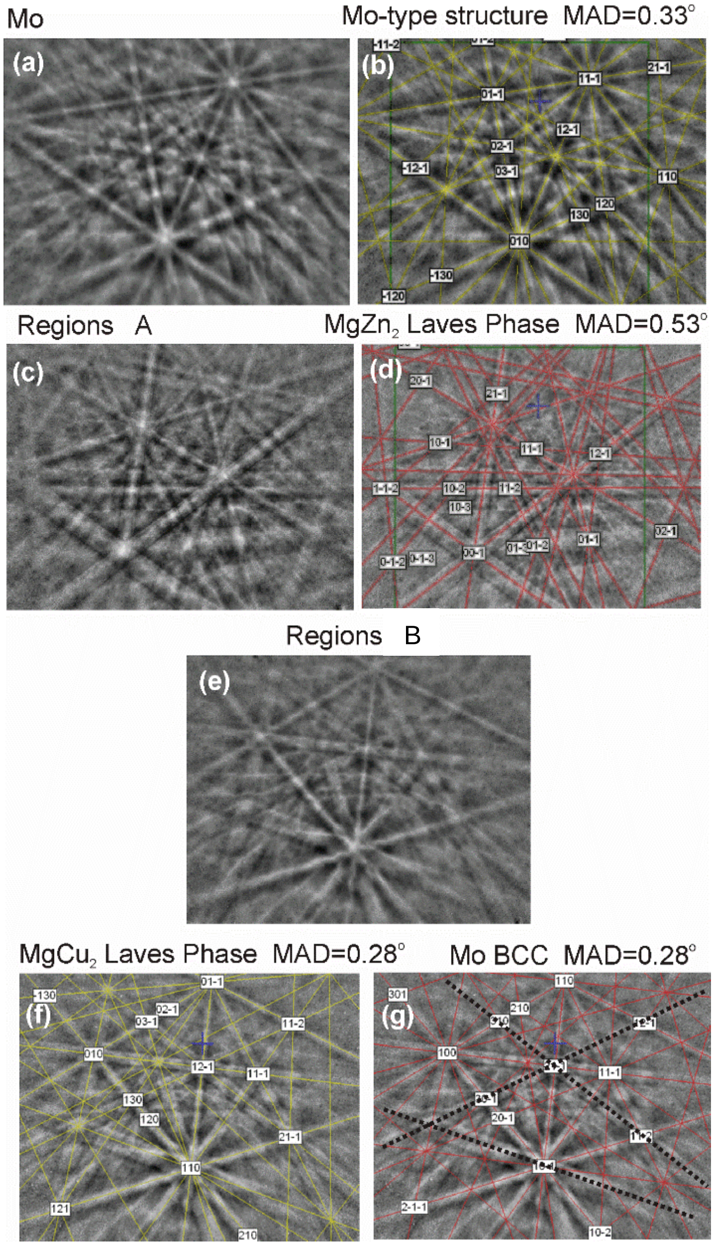

*Figure 4-6 - EBSD experimental pattern for (a) regions **H1**, (c) regions **A1**, (e) regions **B1** and simulated patterns for (b) Mo-type structure, (d) MgZn2 Laves phase and (f) MgCu2 Laves phase and (g) Mo-type structure (BCC). All the simulations were performed using 50 reflectors and 10 bands*

Therefore, the results allow to infer that the crystal structure of regions **B1** seems to have a cubic symmetry, but it is neither the $MgCu_2$ Laves phase nor the BCC phase.

4.2. $CrCu_xFeTiV$

Table 3-2 has a summary of the samples produced for the $CuCr_xFeTiV$ system.

Table 3-2 - Molar ratio and atomic percentage of all the compositions of $CrCu_xFeTiV$ system

Sample	**Cu (at.%)**	**Cr (at.%)**	**Fe (at.%)**	**Ti (at.%)**	**V (at.%)**
x=0.21	5	23.75	23.75	23.75	23.75
x=0.44	10	22.5	22.5	22.5	22.5
x=1	20	20	20	20	20

4.2.1. X-ray diffraction analysis

Figure 4-7 shows the experimental diffractograms for CrCuxFeTiV (x= 0.21 and 0.44) samples. The diffractograms for all samples show peaks for a BCC phase and hexagonal Laves structure (C14) of MgZn2 type. The perfect match with the simulated lattice parameters of the Laves structure and the experimental diffractogram was not possible.

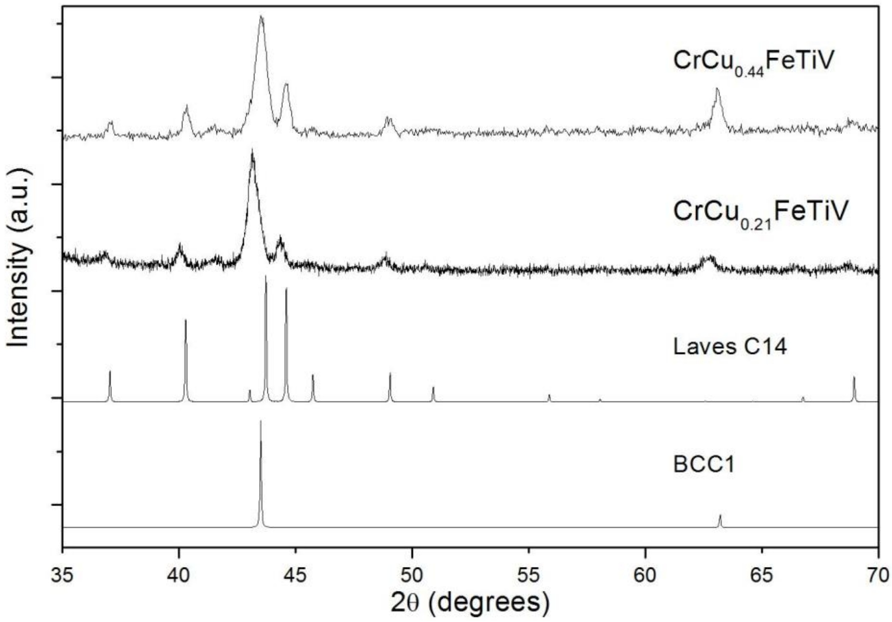

Figure 4-7 - Experimental diffractogram of $CrCu_{0.21}FeTiV$ and $CrCu_{0.44}FeTiV$ alongside simulation of identified peaks.

The CrCuFeTiV sample XRD pattern shows the appearance of new reflections corresponding to two new structures, as seen in Figure 4-8. A FCC structure with a lattice parameter of 0.36234 nm and a BBC (named as BCC2) with a lattice parameter of 0.31465 nm.

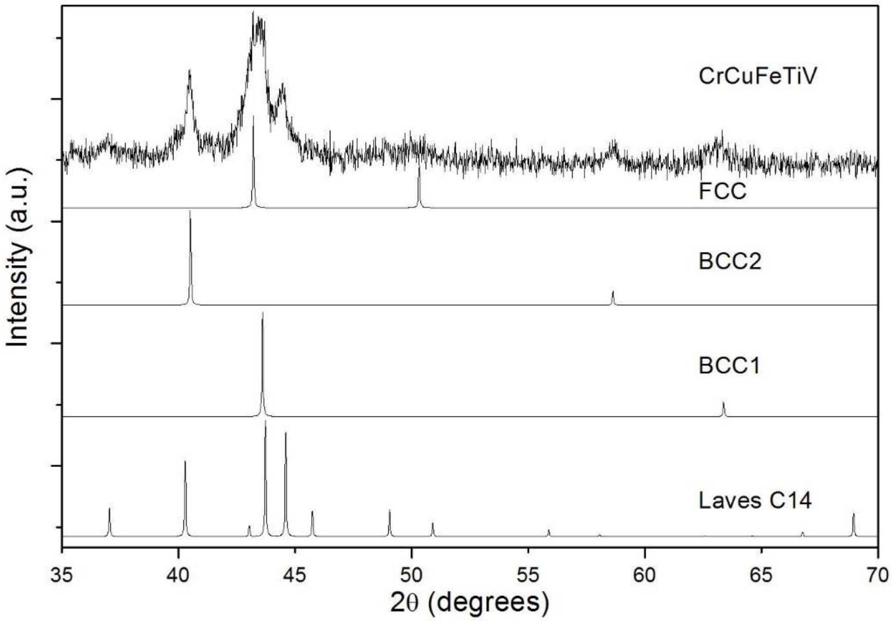

Figure 4-8 - Experimental diffractogram of CrCuFeTiV alongside simulation of identified peaks.

All the identified experimental lattice parameter and prototype phases are resumed in Table 4-3.

Table 4-3 - Experimental lattice parameters

Phase	**Pearson's Number**[93]	**SGR**	**Prototype**	**Parameters (nm)**		
				x=0.21	**x=0.44**	**x=1**
BCC1	cI2	Im-3m	W	a=0.29622	a=2.9400	a=0.29400
Laves C14	hP12	$P6_3/mmc$	$MgZn_2$	?	?	?
FCC	cF24	Fm-3m	Cu	-	-	a=0.36234
BCC2	cF4	Im-3m	W	-	-	a=0.31465

4.2.2. Microstructure analysis

Upon exchanging molybdenum for vanadium in the same system, once again we obtain a multiphasic structure. In Figure 4-9 the microstructure of the three sample are represented with BSE images in low magnification and high magnification. The phases are the same for all three samples, changing the volume fraction between them. There were 5 identified phases: **A2** the grey matrix phase; **B2**, the brighter regions; **C2**, appears close and is similar to **B2**; **D2**, is the darker phase and **E2**, has dark grey hue and is considered as matrix phase also distributed throughout the sample. The results of the EDS analysis are presented in Table 4-4.

Table 4-4 - EDS results for all identified in CrCuxFeTiV.

Regions	**Elements (at.%)**				
	Cu	**Cr**	**Fe**	**Ti**	**V**
A2	4.54±1.24	19.02±0.78	27.88±1.52	30.59±1.05	17.97±1.34
B2	88.68±0.24	0.99±0.2	1.83±0.18	7.36±0.23	1.14±0.14
C2	46.25±1.12	4.2±0.69	10.56±0.39	34.56±0.92	4.43±0.86
D2	7.52±0.86	7.72±0.35	25.46±0.44	48.65±0.65	10.65±0.49
E2	2.37±1.00	32.62±0.44	17.35±0.44	14.19±0.54	33.48±0.42

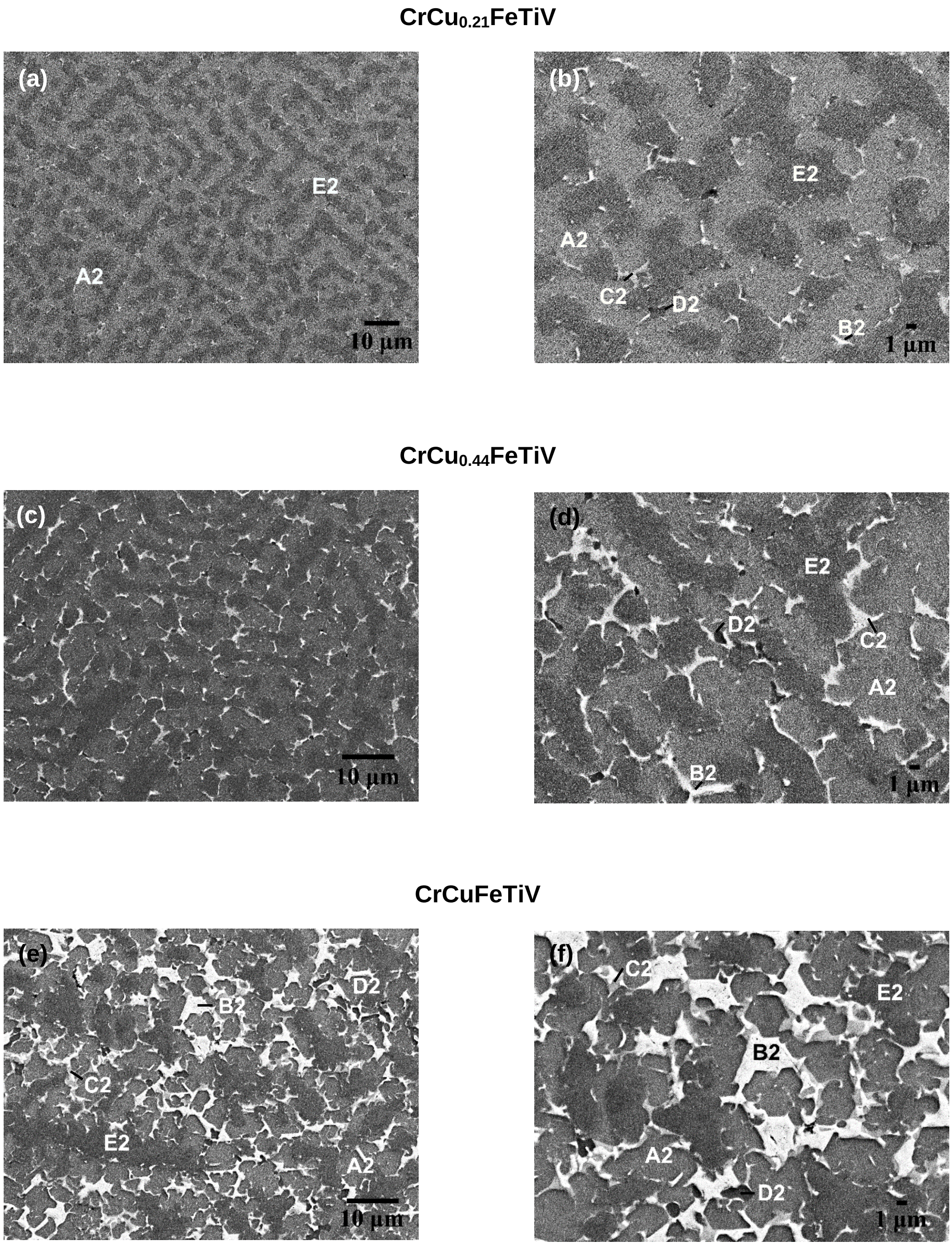

$CrCu_{0.21}FeTiV$

$CrCu_{0.44}FeTiV$

CrCuFeTiV

Figure 4-9 - BSE/SEM images showing the microstructure of CrCuxFeTiV with a) and b) x=0.21, c) and d) x=0.44, e) and f) x=1

4.2.2.1. Matrix phase

It is proposed that both these structures correspond to the main phases **A2** and **E2**, as shown in Figure 4-9.

The Laves phased are characterized for having a compact AB_2 type structure, in which atom A is larger than the atoms that occupy position B. Considering this, we propose that phase **A2** must be the Laves phase as it possesses the correspondent one third of its content as titanium, the element with the largest atomic radius (Table 2-2) [54], occupying the A position of the structure, while the other smaller elements, Cu, Cr, Fe and V (table 3-1) [54] occupy the B positions in the structure.

It is not unexpected as there are C14 type Laves structures in the Fe-Ti; Cr-Ti; Cr-Fe-Ti [119] and Fe-Ti-V[120] systems and Cu [121], Fe [121], Cr [122], and V [123] have been reported to be able to substitute the B position of such C14 Laves phase.

Two phases coexist as the matrix of the sample, labeled phases **A2** and **E2**. As the volume of the **B2**, **C2** and **D2** phases increases, these two major phases become less interconnected, going from a practically continuous phase **A2**, Figure 4-9 (a), to a disconected phase, Figure 4-9 (f).

By consequence, phase **E2** is proposed to be BCC, the second structure that appears in all the $CrCu_xFeTiV$ diffractograms, Figure 4-7 and Figure 4-8, as the other matrix phase present in large quantity in every sample. This solid solution is rich in iron, chromium and vanadium all of wich are BCC. The indexed lattice constants were: 0.2962nm for x=0.21; 0.2940 nm for x=0.44 and 0.2933 nm for x=1. The decrease in lattice size is probably due to a small substitution of copper atoms in the lattice which are of smaller atomic radius.

During preparation of the equiatomic sample for powder XRD, it revealed increase toughness compared to the other samples, using cryogenic grinding to obtain the powder, as stated in Section 3 – Techniques and Procedures. It is proposed that such phenomenon was due to the loss of the continuous **A2** phase, as previously noted in Figure 4-9, which would be particularly brittle, characteristic of Laves phase [111]. The mixture between BCC and FCC phases in the discontinuous Laves phase could be responsible for the toughening mechanism. Chen et al. [112] reported the increase in toughness for two-phase alloys of C14 Laves in a BCC matrix phase, compared with single Laves C14 phase.

4.2.2.2. Dispersed phases

Phases **B2**, **C2** and **D2** have a small volume in the x=0.21 and x=0.44 samples, being accurate EDS readings only possible in the equimolar sample where these phases fraction is larger. The EDS analysis, Table 4-4, reveals that these phases have a very similar composition to phases

B1, **C1** and **D1** of the previously studied $CrCu_xFeMoTi$ system, being the morphology of the copper rich **B2** different.

Another notable phase evolution, is that increased copper content leads to an increase in volume fraction of these phases **B2**, **C2** and **D2**. As seen in the microstructure changes in Figure 4-9. The addition of copper to the system did not promote the formation of new phases. Indicating that added copper is not dissolved in the existing phases and promotes a change in the overall volume fraction of the phases.

In composition x=0.21, phase **C2** is noted around phase **E2**, together with small grains of **B2** and **D2**, (Figure 4-9 (a) and (b)), perhaps **C2**’s nucleation is dependent on phase **E2**. As we increase copper content to x=0.44, the three phases, **C2**, **D2** and **E2** increase, although, **C2** remains the more relevant, (Figure 4-9 (c) and (d)), still surrounding phase **E2**. Upon reaching the equimolar composition, x=1, phase **B2** becomes the most relevant of the three.

As noted in Figure 4-10, the $CrCu_{0.44}FeMoTi$ (a) sample the white **B2** copper rich regions tend to show up like long dendrites, while the CrCu0.44FeTiV (b) sample has the equivalent white **B1** regions as patches between the grains of the matrix phases. In the vanadium system it looks like copper rich phases form as they separate from the **E2** phase while in the Mo system copper phases originate directly from the matrix phase **A1**. It was also reported that titanium and vanadium additions could promote copper separation [124].

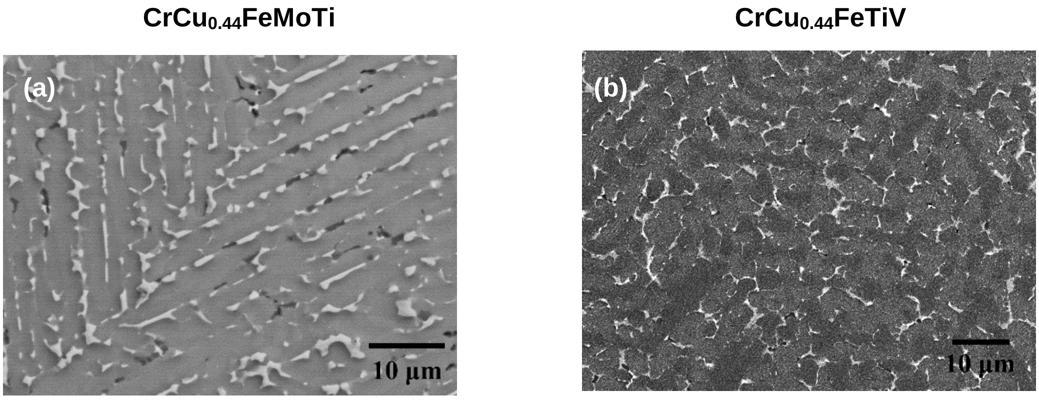

Figure 4-10 - Comparison of morphology of copper rich regions between the $CrCu_{0.44}FeMoTI$ (a) and $CrCu_{0.44}FeTiV$ (b)

For the CrCuFeTiV diffractogram two new peaks are detected, the FCC and BCC2, Figure 4-8. These new peaks likely correspond to two of the three phases, **B2**, **C2** or **D2**, whose volume percent is now large enough in the equimolar sample to be detected on the XRD.

The FCC phase can be associated to phases **B2** and/or **C2** as they are copper rich, and its parameter is similar to the one of pure copper, 0.36146 nm. The **D2** phase rich in titanium could be the BCC2 structure, attributed to a beta titanium solid solution, lattice of 0,33065nm, Table 2-2, in which the large addition of other elements reduced the lattice parameter.

The X-ray map (Figure 4-11) reveals the distribution of the elements in the equimolar sample, which contains the larger volume fraction of each phase. Results agree with EDS point analysis, revealing copper rich phases and the distribution of Fe, Cr and V.

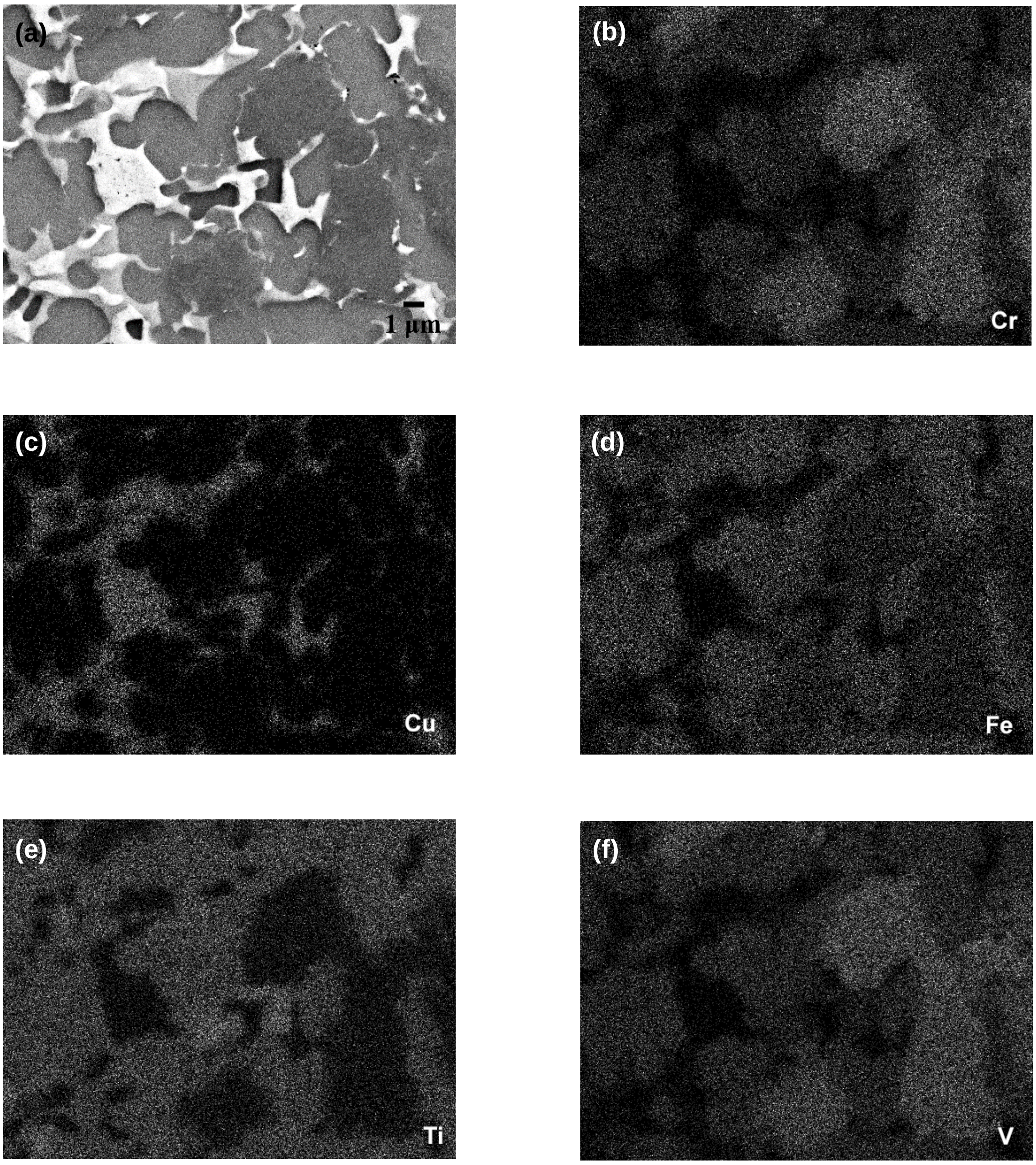

Figure 4-11 - X-ray map of CrCuFeTiV

4.2.3. Phase prediction models

All samples exhibited multiphasic structures, although the equimolar sample presents the highest possible entropy of mixing, by the Boltzmann's hypotheses [23], there was no tendency to create a single phase. It has already been discussed that the entropy effect is not the only effect in play in stabilizing metastable simple solid solution phases, and that the entropy may be useful to rationalize the formation of solid solutions, but not to predict them [35]. The other relevant factors proposed to predict the structures that high entropy alloys will form are mainly the atomic size difference (δ), the enthalpy of mixture (ΔH_{mix}), the Valence Electron Concentration (VEC) and the electronegativity (χ) [55]. S. Guo et al. compiled the results of the microstructures of multiple HEA systems to create an empirical relation between δ, ΔH_{mix} and the structure that will be formed [47]. The proposed relation is represented in figure 3-1 alongside the calculated values for the system of this study. The studied system falls within the proposed relation, having obtained both solid solutions and an intermetallic phase.

The absence of single phases solid solution could be due to atomic size differences. As it has already been discussed, this limit can be imposed by atomic size differences. Guo et al. [125] have attempted to show the effect of this increased mismatch. However, they used copper which lead to an already expected phase separation, so their results do not represent the complete truth. As per the schemes in Figure 2-9 we notice that the alloy is in the region of formation of solid solutions and intermetallic compounds.

4.3. Isolation of the composition $Cu_{0.17}FeCrMo_{0.17}Ti$

In order to obtain the measurement of the thermal properties of these alloys and understand the nucleation of ordered phases, a sample with $Cu_{0.17}FeCrMo_{0.17}Ti$ composition was prepared based on the EDS results of the matrix phase **A1**. An almost single-phase sample, just containing traces of other minor phases was obtained, as shown in Figure 4-12. In Table 4-5 is presented the EDS

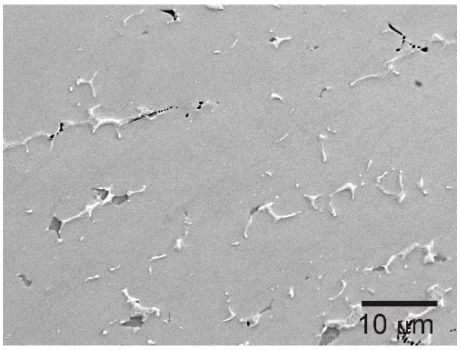

Figure 4-12 – Microstructure of the Cu0.17CrFeMo0.17Ti sample.

results of the major phase, since the other phases did not present extended areas to perform accurate analysis.

The elemental analysis reveals a matrix phase relatively similar in composition to the **A1** phase in the previous system. Less copper percentage than the nominal composition (5 at% Cu) of the alloy is detected, meaning that the minor phases observed are probably phases based on copper. Possibly of the types of phases **B1**, **C1**, **D1** and **E1**, based on the observation of the backscattered image in Figure 4-12. This shows us that even reducing the molybdenum content, and by consequence the interaction of Cu-Mo, a simple structured solid solution of all the components could not still be achieved.

Table 4-5 - EDS results for matrix phase observed in the isolated sample.

Regions	**Elements (at.%)**				
	Cu	**Cr**	**Fe**	**Mo**	**Ti**
Matrix	1.64±0.2	27.23±0.3	32.50±0.29	4.26±0.33	34.37±0.38
A1	2.67±0.42	31.28±1.6	33.05±1.92	7.55±1.54	25.46±1.19

In Figure 4-13 the XRD results for sample $Cu_{0.17}FeCrMo_{0.17}Ti$ is presented. It reveals, as expected, the presence of a hexagonal Laves phase.

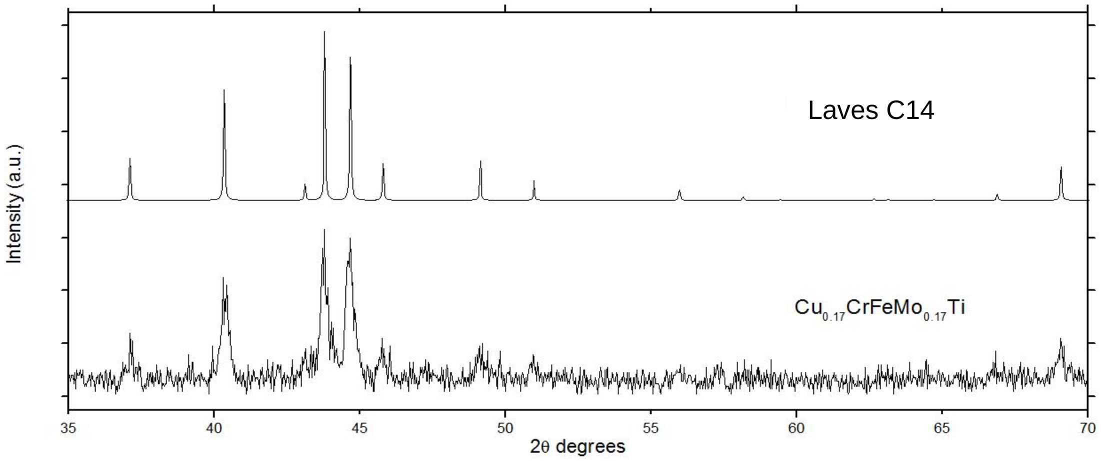

Figure 4-13 - diffractogram of Cu0.17FeCrMo0.17Ti evidencing the majority phase as a hexagonal Laves phase.

Results of thermal diffusivity versus temperature measurements made on the $Cu_{0.17}FeCrMo_{0.17}Ti$ sample are shown in Figure 4-14. The $Cu_{0.17}FeCrMo_{0.17}Ti$ evidence low diffusivity values when compared to W (0.5-0.7 cm^2/s) [126] and CuCrZr (0.9-1 cm^2/s) [127] for the 425-875 K range, which slightly increase with temperature. Previous reported studies in HEA [74][38] the thermal diffusivity also increases with increasing temperature.

This behavior is opposite to what is seen in most of the pure metals. The enhanced heat transfer at high temperatures for high entropy alloys was explained by the increased phonon mean free path at higher temperatures, owing to the thermal expansion of the lattice [74][38]. Therefore, results indicate that this isolated Laves phase has good thermal properties. A fully disordered HEA phase as a whole could provide thermal properties together with the others needed, having a good potential to be applied as thermal barriers for fusion reactors.

Table 4-6 - Lattice parameter of indexed peaks

Phase	**Pearson's Number**[93]	**SGR**	**Prototype**	**Parameters (nm)**
Laves C14	hP12	$P6_3/mmc$	$MgZn_2$	a=0.48418 c=0.79165

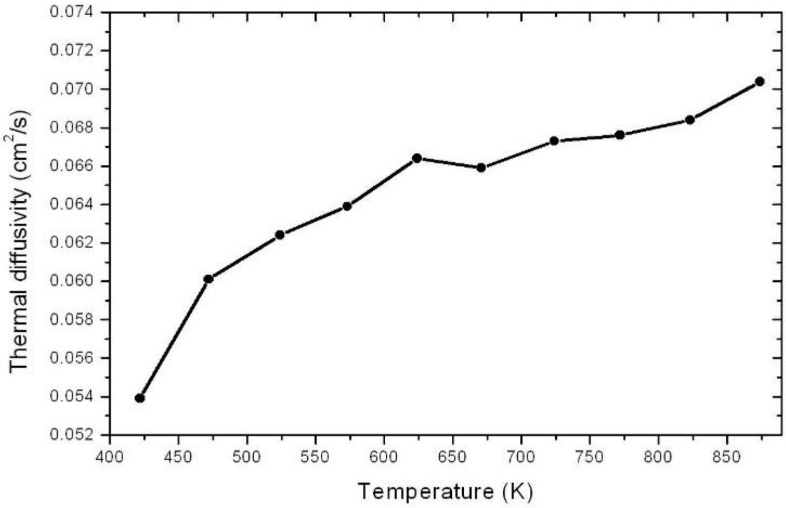

Figure 4-14 – Thermal diffusivity measurements in sample Cu0.17FeCrMo0.17Ti.

4.4. Conclusion

The $CrCu_xFeMoTi$ and $CrCu_xFeTiV$ (x= 0.21, 0.44, 1) high entropy alloy systems were produced by arc melting. Unlike what it was expected, the observed microstructures were not simple and with small number of phases. Up to 8 phases were present in Mo containing system and 5 for the V containing one.

Segregation of molybdenum occurred in all three samples of $CrCu_xFeMoTi$, leading to a depletion of Mo in the melt and by consequence the formed structures. This was attributed to solidification kinetics and coefficient of partition due to the high melting point of Mo compared with the other elements.

In the $CrCu_xFeTiV$ system, no large segregation of species was noted to the same level of the other system, but the matrix phase was separated between an ordered Laves phase and BCC solid solution.

The increase in copper content did not lead to its dissolution within the formed phases, instead it increased the volume fraction of copper rich structures in both the systems. The formation of these copper rich structures is associated with the high binary enthalpy of mixture of copper with the remaining metals. This promotes phase separation and decreases likelihood of formation of single phases. Both systems contained as the matrix phase an ordered C14 Laves phase because of the interaction of titanium with the other elements.

The expected entropy effect was not verified for these systems as the metastable solid solutions did not dominate over the remaining phases. It is proposed that a reduction of the atomic ratio of both copper and titanium, could promote simpler structures, by preventing phase separation of copper rich phases and reducing the tendency of ordering the Laves phase structure.

An almost single phase $Cu_{0.17}FeCrMo_{0.17}Ti$ sample was also prepared, evidencing low diffusivity values in the 425-875 K temperature range.

5. Solid Route – Results and Discussion

The results and discussion of the CrCuFeTiV-MA sample, produced by powder metallurgy are described in the next section. Comparison between the solid route and the liquid route from the previous section is discussed. The effect of ion beam irradiation on the structure is also analyzed.

5.1. As-sintered

The production of the CrCuFeTiV-MA sample involved mechanical alloying to obtain the homogenous mixture of the elements. After the milling the powder was sintered by spark plasma sintering, to which microstructure and XRD analysis were performed.

5.1.1. Microstructure analysis

Secondary electron images of the microstructure of the as-sintered sample are displayed in Figure 5-1. The sample has very fine microstructure, phases being around 1μm in size, indicating sub micrometric grain size. Three phases can be identified, noted as **A**, **B**, and **C** in Figure 5-1, and the corresponding EDS analysis is presented in Table 5-1.

According to EDS point analysis, region **A** is a copper rich phase. Phase **B** is depleted in copper but is richer in chromium and poorer in titanium. Phase **C** is distributed throughout the whole sample, it has less copper content and an approximate similar distribution of the remaining element in the composition, which places it still within the HEA composition definition.

Throughout the sample small black spots are observed. These resemble nanoporosity, as noted in the SE images of the sample tilted at 70º in Figure 5-2 . This porosity is a lot less prevalent in phase A and B, but is more common throughout the matrix phase C.

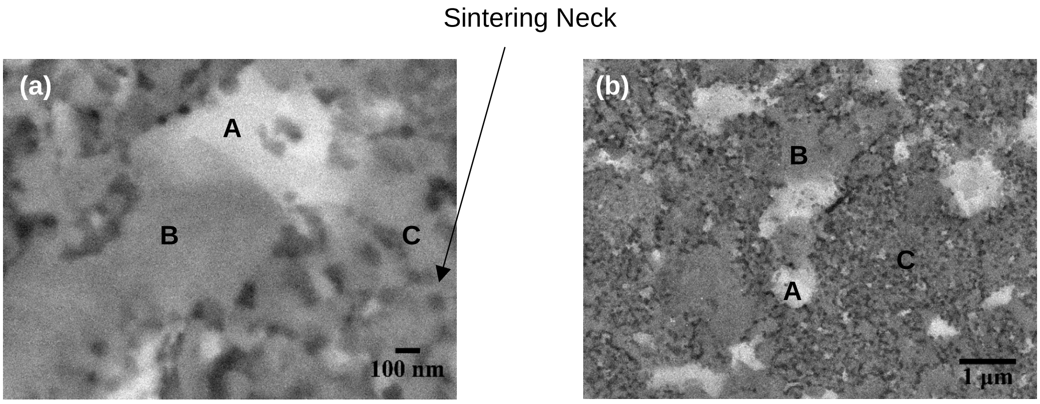

Figure 5-1 - SE micrographs of the surface of the consolidated sample

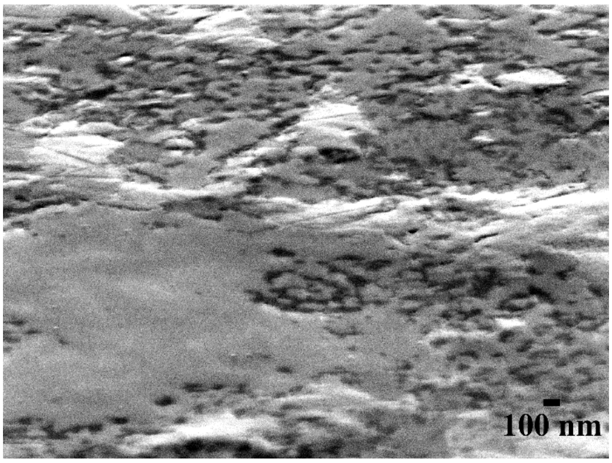

Figure 5-2 - SE micrograph tilted at 70º revealing detail of porosity

Table 5-1 - EDS analysis in the phases denoted as A, B and C belonging to the CrCuFeTiV high entropy alloy.

Regions	**Elements (at.%)**				
	Cu	**Cr**	**Fe**	**Ti**	**V**
A	71.28±9.57	7.12±3.24	7.28±1.77	7.32±1.58	7.00±3.07
B	6.63±4.37	34.94±3.03	25.91±2.34	9.86±2.05	22.69±2.77
C	7.44±2.13	23.16±2.55	25.01±1.13	22.44±3.03	21.95±1.03

5.1.2. X-ray diffraction analysis

Figure 5-3 displays the grazing incidence diffractogram of the CrCuFeTiV-MA sample and the corresponding simulated patterns. Two FCC structures were identified, denoted as FCC1 and FCC2. The first with a lattice of 0.35267 nm and the latter with 0.36145 nm. The details are summarized in Table 5-2.

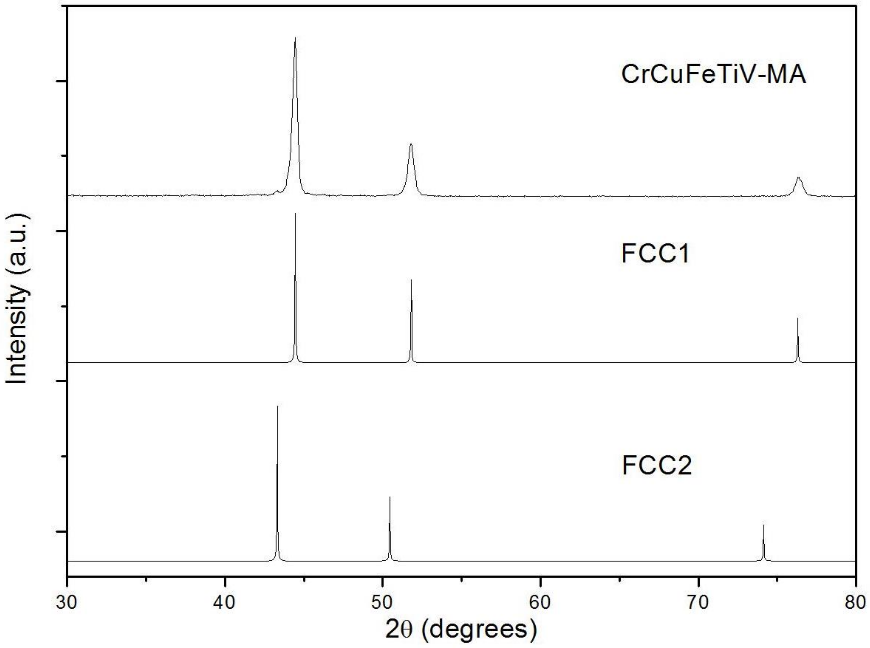

Figure 5-3 - Experimental GXRD pattern of CrCuFeTiV-Ma and simulated patterns

Table 5-2 - Identified structures and lattices parameters by GXRD of CrCuFeTiV-MA

Phase	**Pearson's Number**[93]	**SGR**	**Prototype structure**	**Parameter (nm)**
FCC1	cF4	Fm-3m	Cu	0.35267
FCC2	cF4	Fm-3m	Cu	0.36146

The same sample once grinded and analyzed with PXRD unexpectedly revealed different results. This method revealed the appearance of an FCC, BCC and an unidentified phase, illustrated in Figure 5-4. Small intensity peaks of WC were also identified and is due to the WC container used in the grinding. Identified phases are summarized in Table 5-3.

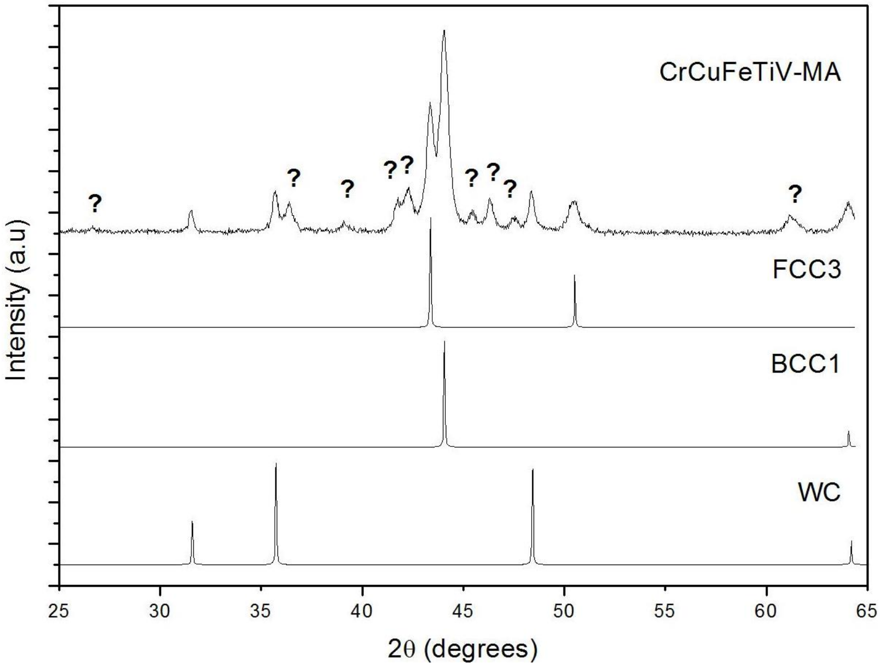

Figure 5-4 – PXRD diffractogram of CrCuFeTiV-MA and simulated patterns

Table 5-3 - Identified structures and lattices parameters by PXRD of CrCuFeTiV-MA

Phase	**Pearson's Number**[93]	**SGR**	**Prototype structure**	**Parameter (nm)**
BCC1	cI2	Im-3m	W	a=0.2905
FCC3	cF4	Fm-3m	Cu	a=0.36116
WC	hP2	P-6m2	WC	a=0.29060 c=0.28370

The diffractograms of the bulk and powder XRD method is represented in Figure 5-5. Between the two, the phases FCC1, for GXRD, and the FCC3, for PXRD are practically equal, indicating after grinding this FCC phase remains constant.

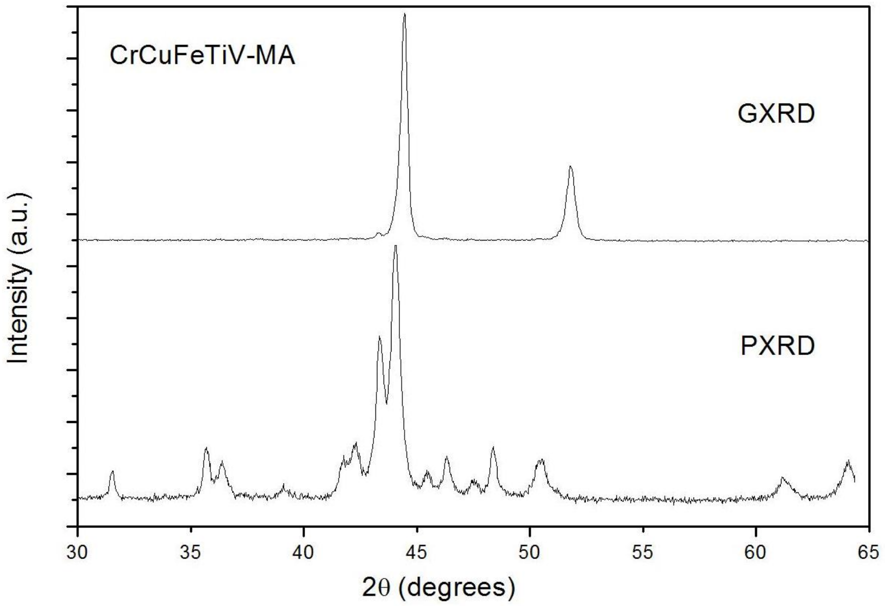

Figure 5-5 - Comparison of XRD diffractograms obtained by GXRD and PXRD

5.2. Argon irradiation

A CrCuFeTiV sample was irradiated with Ar ions with an energy of 300keV to the fluence of $3x10^{16}$ at/cm^2. The surface changes in the microstructure and crystalline structure are presented in the next section. This sample is denoted as CrCuFeTiV-imp.

5.2.1. Microstructure analysis

Noticeable changes in microstructure are not observed, no blistering, swelling or fissuration was present. The only observed change in the microstructure was the formation of craters which may be due to the erosion caused by the Ar ions, only observable at 70º angle. From this tilt we can also observe the nanoporosity already present in the previous micrographs. The same three phases were observed and EDS results remained similar to the as-sintered sample.

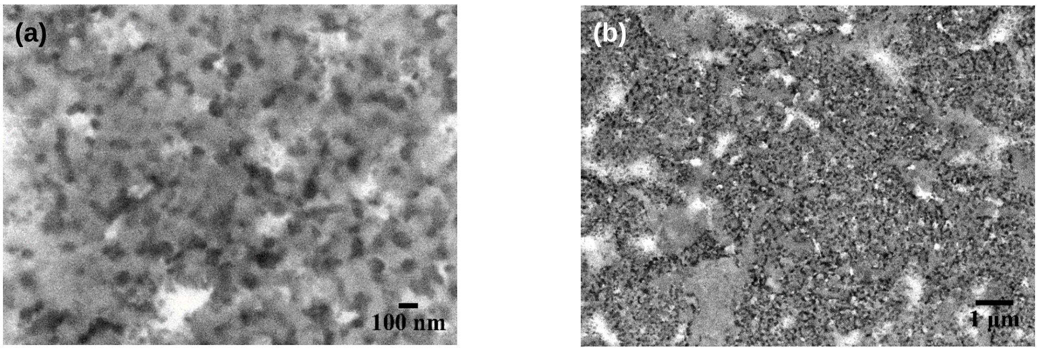

Figure 5-7 - Surface of irradiated sample

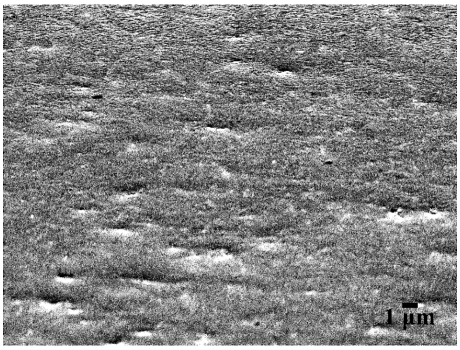

Figure 5-6 - 70º tilted image of irradiated sample. The grooves observed are craters resulting from the irradiation

5.2.2. X-ray diffraction analysis

The effect on the crystal structure was revealed with grazing incidence XRD analysis. The experimental pattern is represented on Figure 5-8. The structure is composed of an FCC structure, a BCC and an unidentified structure. The identified samples are described in Table 5-4.

Interestingly the irradiated sample, reminisces more to the powder analysis rather that the grazing analysis of the non-irradiated sample. This becomes clearer when comparing directly the three, present in Figure 5-9.

Table 5-4 - Identified structures and lattices parameters by GXRD of CrCuFeTiV-imp

Phase	**Pearson's Number**[93]	**SGR**	**Prototype structure**	**Parameter (nm)**
BCC2	cI2	Im-3m	W	a=0.29150
FCC4	cF4	Fm-3m	Cu	a=0.36146

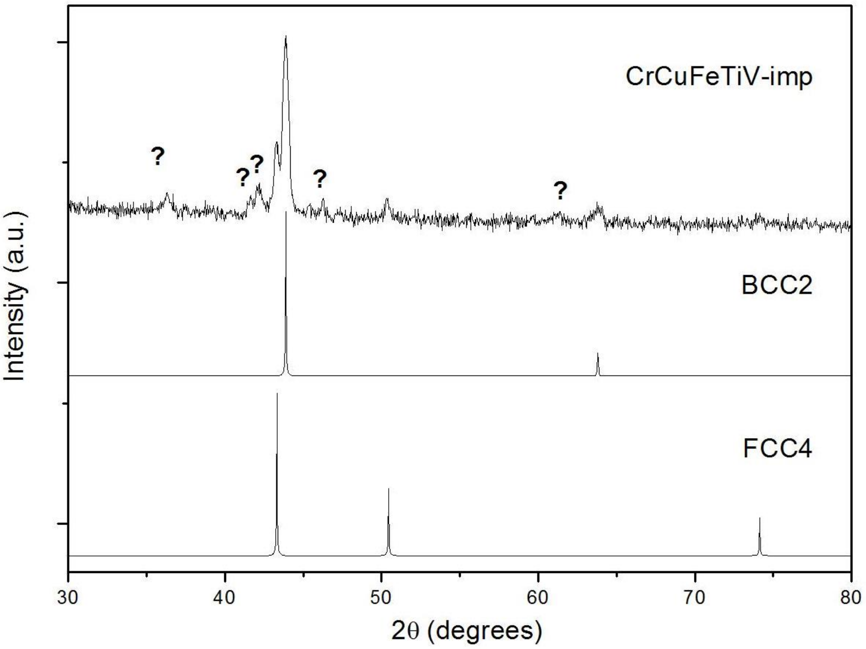

Figure 5-8 - GXRD pattern of CrCuFeTiV-imp and simulated patterns

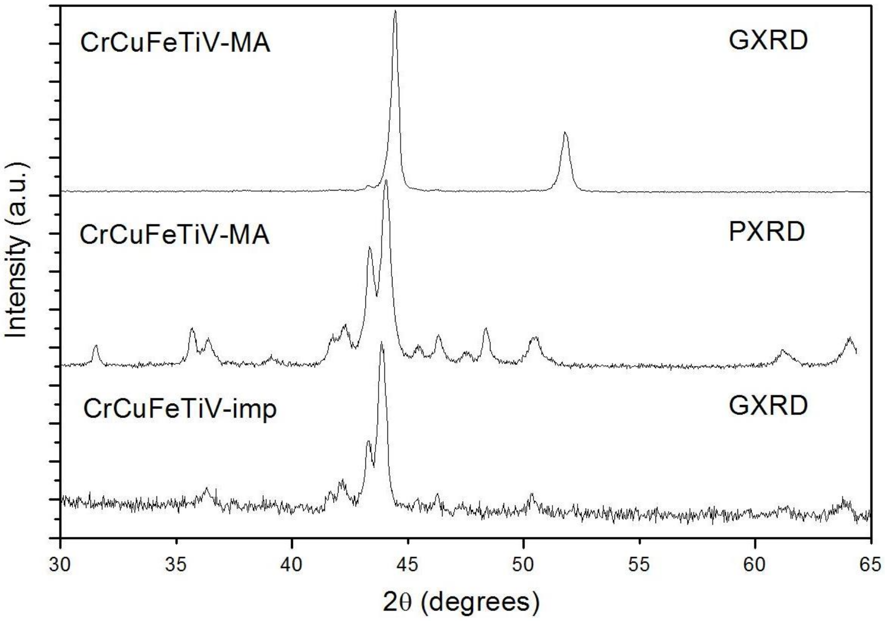

Figure 5-9 - Comparison of the three obtained diffractograms. GXRD and PXRD for non-irradiated. GXRD for irradiated

5.3. Discussion

The results of the sample produced by sintering are discussed in this section.

5.3.1. XRD analysis and discrepancies

All three XRD analysis, GXRD and PXRD of CrCuFeTiV-MA and the GXRD of CrCuFeTiV-imp, contain a small peak probably corresponding to a FCC structure. The lattice parameter is quite similar between the three analyses, ranging from 0.36116 nm to 0.36146 nm. Considering that the lattice parameter of pure copper is 0.36146 nm, it is possible that the small copper rich patches present in the microstructures correspond to this FCC peak. The summary of all XRD analysis in Table 5-5, shows that this copper rich FCC phase remains unchanged throughout every process applied to the sample.

When comparing the CrCuFeTiV-MA sample analyzed by GXRD or PXRD, the surface analysis reveals a strong FCC1 peak, while the powder reveals a BCC1 and other unidentified peaks. Phase **B**, which span through a large region of the sample can give a larger signal for having a large volume and be associated to these stronger peaks FCC in the GXRD and to the BCC in the PXRD. On the other hand, the parameter of the CrCuFeTiV-MA PXRD BCC structure is similar to the one of chromium, being this structure chromium rich Table 5-1.

Figure 5-10 represents the diffractogram of an annealed sample, revealing that the CrCuFeTiV-MA structure remains unchanged. As such the FCC to BCC transformation could be attributed to a martensitic transformation, consequence of the grinding performed to turn the sample into

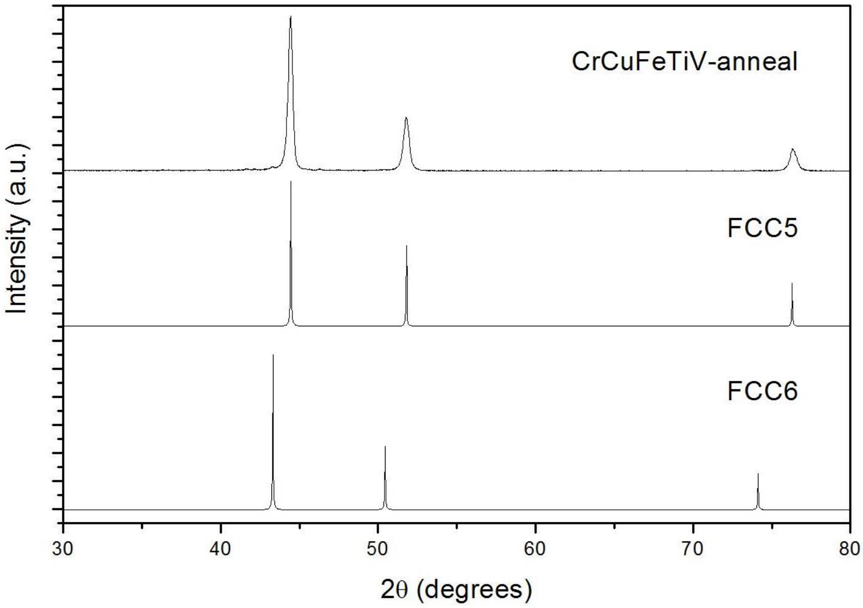

Figure 5-10 – GXRD analysis of the annealed CrCuFeTiV non-irradiated sample powder. The mechanical action would give energy to the atomic planes to perform the transformation.

The unidentified peaks could have already been present in the sample and enhanced or were formed by the mechanical grinding for the PXRD and effect of ion irradiation.

Phase **C** due to its higher Cr content and small volume, one can infer that it possesses a minor BCC peak hidden by the major FCC1, similarly noted in by Praveen et al. [128], in which a minor BCC structure is identified in alloys with FCC formation affinity because of the added Cr.

Table 5-5 – Summary of all the XRDs performed on the sintered, irradiated and annealed sample

CrCuFeTiV-MA-GXRD

FCC1	0.35267
FCC2	0.36146

CrCuFeTiV-MA-PXRD

BCC1	0.29050
FCC3	0.36116

CrCuFeTiV-imp-GXRD

BCC2	0.29150
FCC4	0.36146

CrCuFeTiV-anneal-GXRD

FCC5	0.35283
FCC6	0.36146

5.3.2. Phase formation

Phase formation in HEAs produced via powder metallurgy is mostly defined during the mechanical alloying step. Studies reveal that the main factor controlling alloying is the melting temperature, followed by the crystal structure and mechanical properties [68] [70]. Higher melting temperature elements possess stronger atomic bonding, making it more difficult for the elements to mix in a single alloy, affecting the solid solubility. Moreover, soft FCC structures will lead to easier alloying by covering the other elements through plastic deformation during milling. For our system composed of CrCuFeTiV, based on this, one can venture that the alloying order could be Cu – Fe – Ti – Cr – V.

In the microstructure, regions enriched in copper are observed as **A** regions. Copper being the lowest melting temperature present in the mixture and being the only one with the softer FCC structure, its incorporation should be practically guaranteed upon milling. However, in our case it is clearly observed an incomplete dissolution of copper in the alloy. This lack of solubility can be then attributed to the high enthalpy of mixture of copper with the other transition metals, which prevents mixing of copper or can lead to its separation during the SPS process. Mridha et al. [129] reported the formation of Cu based FCC and Cr based BCC solid solutions upon milling. Formation of such copper rich regions in equimolar alloys containing copper produced by SPS, have been reported by other authors [37], [73], [128], [130].

Unfortunately, XRD analysis of the milled powder before sintering, was not possible. This would have cleared if the copper had dissolved during the MA process and then separated during SPS. Praveen et al. [128] have shown that for 15 hour milling AlCoCrCuFe alloy will form a major BCC phase with a minor Cu rich FCC phase, while the NiCoCrCuFe reveals the opposite a major FCC phase with a minor BCC. The authors [128] milled other compositions revealing that Cu was responsible for stabilizing an FCC phase while Al and Cr were responsible for the BCC phases.

Moreover, the small grains of the consolidated sample are related to the nature of the MA process that promotes fine grains, already proven to be very stable in HEA when subjected to high temperatures, probably due to slow grain growth kinetics due to the low diffusivities among the elements in the multicomponent solution [131]. This coupled with the fast consolidation by SPS in minutes rather than hours when compared with conventional sintering methods, extensive grain growth is prevented [72],[73], and the fine structures can be retained.

When comparing with the liquid route equimolar sample, analyzed in the previous section, Figure 4-9, a lower number of phases are identified via the solid route. The microstructure is coarser when solidifying, and the multitude of dispersed phases based on copper and titanium are not observed when sintering. A lack of Laves phase in this sample, is likely related to the nature of the milling, which with its constant impacts prevents the formation of ordered phases [132]. The unidentified structure with a lower signal in both the as-sintered PXRD and irradiated GXRD, Figure 5-9, is most likely an ordered structure with low symmetry due to its large number of reflections. However, without XRD analysis from the milled powder it is not possible to explain the origin accurately.

5.3.3. Microstructure topography

Both phases A and B do contain a lot less observable nanoporosity when compared with phase C. SPS is a fast consolidation process that makes use of pulsed electric current, the consolidation is promoted by the localized high temperatures at the surface of the powders and discharges between then. It was proposed to have 4 stages in metallic samples [85]: 1) activation and refining of powders – spark discharges between particles remove impurities from their surfaces; 2) formation and growth of sintering neck – local high temperature melts or even vaporizes the metal and creates necks by sputtering or diffusion; 3) rapid densification – the current passing leads to joule heating which promotes diffusion; 4) plastic deformation densification – the application of pressure during the process together with the high heat softening of the boundaries leads to densification. Noting the arrow in Figure 5-1(a), pointing to the joining necks between the grains in phase **C**, indicates that the necks connecting the grains in phase C have indeed formed, one can infer that something must have hindered the two final sintering steps, the extensive mass transport phenomena and plastic deformation that would close most remaining pores [86].

Song et al. [87] proposed a self-adjusting neck formation mechanism, that aims to explain the formation of homogenous necks throughout consolidated samples in conductive metals. The work suggests that as the die possesses a larger resistivity than the copper powder, most current must pass through the sample. Within the sample it will choose the path of least resistance, such as grains with larger contact areas, leading to neck formation and coarsening in such regions. However, at elevated temperatures the resistivity of copper increases in these localized regions, becoming other contact regions paths of less resistance. In this way, the initial formation and growth of necks are dependent on the competition of resistivity and contact area.

It is possible that in the beginning of the process neck formation occurred normally between the original powder mixture, whether by coarsening or spark discharges [88], while copper began segregating and forming its enriched regions. Upon phase A appearance, it could have started “hogging” the electric current. As copper possesses the lowest resistivity of all the elements and a multicomponent mixture could be highly resistive [45], [74], it could have hindered the passing of current throughout the other phases. Concerning the phase B also fully consolidated, it could be that the heat extraction of copper lead to enhanced diffusion and sintering near regions consolidating the B phase, or as the resistivity of copper increased the next path of least resistance was B’s multicomponent mixture, but never phase C. Being that upon neck formation, joule heating responsible for the growth of the neck [85], will not occur greatly on phase C and the applied pressure is not probably enough to promote plastic deformation to aid in the consolidation. One must be reminded that the sintering occurred at holding time of 5 min at 900 ºC, having the process not lasted more than 25 minutes including heating and cooling, this time is not enough for full consolidation of neither conventional nor multicomponent alloys by regular methods using only heat. Other studies with multicomponent alloys that also revealed copper rich regions and nanoporosity [72], [128].

5.3.4. Irradiation effect

The only noted changes in the microstructure was the formation of craters, which could be due to the sputtering effect of the argon ions, Figure 5-6. The fact that no blistering, swelling or fissuration is observed may indicate low retention of the ions.

The as-sintered sample reveals clean peaks, Figure 5-3, with very low noise whereas the irradiated sample has a lower signal-to-noise ratio, Figure 5-8, this is probably due to the disorder induced in the structure by the collision of the ions. It is possible for metals to become amorphous when subjected to ion beams, if the free energy of the crystal increases due to the increase of radiation induced defects [133] and the greater atomic strains in concentrated solutions in HEA can lead to amorphization by irradiation easier [77]. The GXRD does not reveal full amorphization but indicates that there has been some structural disorder induced during irradiation.

It seems that the heavy argon ions induced phase transformation observed from FCC (as-sintered) to BCC. Although nanomaterials do possess large defect sinks (high density of grain boundaries) where interstitials and vacancies can anhilate, the multicomponent crystal may not allow elimination of such defects leading to the crystalline structure to change to a BCC phase. This phase transformation, may indicate that the original major FCC1 phase was heavily strained from the MA, and the SPS was able to maintain this out of equilibrium phase. Upon irradiation, sufficient energy was given to the atoms to move to more relaxed position, originating a BCC structure with a much more open structure.

In fact, the similarity of the PXRD structure, Figure 5-9, to the the CrCuFeTiV-imp diffractogram, relates the phase transformation during irradiation to a martensitic phenomenon that happens during grinding.

6. Conclusions and future work

The compositional and production method on two high entropy alloy compositions were studied. Three samples varying the copper content of the CrCuFeMoTi and of the CrCuFeTiV system, totaling six samples, were produced by vacuum arc melting. One equimolar sample of CrCuFeTiV was produced by mechanical alloying followed by spark plasma sintering. This latter sample was submitted to ion beam irradiation.

The pursued sample of a single phase metastable solid solutions in HEA compositions was not obtained. The expected entropy effect was not verified for these systems as this solid solution did not dominate over the remaining phases. The produced samples then are multiphasic. The vacuum arc melt samples contained up to eight phases while the sintered sample remained with only three.

The increase in copper content in the vacuum arc melting samples did not lead to its dissolution within the formed phases, instead it increases the volume fraction of copper rich structures in both the systems. The formation of these copper rich structures is associated to the high binary enthalpy of mixture of copper with the remaining metals. This promotes phase separation and decreases likelihood of formation of single phases. Both systems contained as the matrix phase an ordered C14 Laves phase because of the high interaction of titanium with the iron and chromium.

Segregation of molybdenum occurred in all three samples of CrCuFeMoTi produced by arc melting, leading to a depletion of Mo in the melt and by consequence the formed structures. On the other hand, the CrCuFeTiV system had no large segregation of species but the matrix phase was separated between an ordered Laves phase and BCC solid solution.

An isolation of the Laves C14 matrix phase of the CrCuFeMoTi system produced by arc melt, was done by preparing a sample with the corresponding stoichiometry of the phase. It revealed a microstructure close to monophasic, with traces of copper rich phases. Thermal diffusivity of the sample is low when compared with tungsten and CrCuZr, increasing slightly with temperature

The sintered sample, revealed a very fine microstructure, imparted by the mechanical alloying process and retained during the sintering. Nanoporosity was distributed throughout the matrix phase, which was a simple FCC structure that was depleted in copper. This copper was present in small patches.

The irradiation did not create swelling or fissuration in CrCuFeTiV sample produced by SPS, just craters. A phase transformation from FCC to BCC was detected by XRD in the grinded sample and irradiated sample. This reveals that the original structure was heavily strained due to the milling, and the knock-on effect of the ions pushed the atoms more relaxed positions, leading to the phase transformation.

It is proposed that for future compositions a reduction of the atomic ratio of both copper and titanium, could promote simpler structures, by preventing phase separation of copper rich phases and reducing the tendency of ordering the Laves phase structure during solidification. In the case of the mechanically alloyed sample, increase of milling time could “force” the dissolution of copper or once again reducing it altogether. Studies of milling time and XRD analyses of milled powder should be done. Transmission electron microscopy will confirm the crystal structure of the phases and identify more clearly defects imparted on the sample by the irradiation. Further thermal studies are required, in order to extract more accurate thermal diffusivity and thermal stability of the phases.

7. References

[1] N. Baluc *et al.*, “Status of R&D activities on materials for fusion power reactors,” *Nucl. Fusion*, vol. 47, no. 10, pp. S696–S717, 2007.

[2] ITER.org, “Divertor.” [Online]. Available: https://www.iter.org/mach/divertor. [Accessed: 31-Oct-2017].

[3] K. Sugiyama *et al.*, “Deuterium inventory in the full-tungsten divertor of ASDEX Upgrade,” *Nucl. Fusion*, vol. 50, no. 3, p. 35001, 2010.

[4] V. Barabash *et al.*, “Materials challenges for ITER - Current status and future activities,” *J. Nucl. Mater.*, vol. 367–370 A, pp. 21–32, 2007.

[5] X. Zhang, Q. Yan, S. Lang, M. Xia, X. Liu, and C. Ge, “Thermal shock and fatigue resistance of tungsten materials under transient heat loading,” *J. Nucl. Mater.*, vol. 455, no. 1, pp. 537–543, 2014.

[6] D. Stork *et al.*, “Developing structural, high-heat flux and plasma facing materials for a near-term DEMO fusion power plant: The EU assessment,” *J. Nucl. Mater.*, vol. 455, no. 1–3, pp. 277–291, 2014.

[7] A. Li-Puma, M. Richou, P. Magaud, M. Missirlian, E. Visca, and V. P. Ridolfini, “Potential and limits of water cooled divertor concepts based on monoblock design as possible candidates for a DEMO reactor,” *Fusion Eng. Des.*, vol. 88, no. 9–10, pp. 1836–1843, 2013.

[8] T. R. Barrett *et al.*, “Enhancing the DEMO divertor target by interlayer engineering,” *Fusion Eng. Des.*, vol. 98–99, pp. 1216–1220, 2015.

[9] W. Shen, P. Li, C. Zhou, S. Xu, and S. Wang, “Design and preparation of water-cooled plasma-facing mockups with diamond/copper composite interlayer,” *Fusion Sci. Technol.*, vol. 66, no. 1, pp. 260–265, 2014.

[10] V. . Blank *et al.*, “A new carbon structure formed at MeV neutron irradiation of diamond: structural and spectroscopic investigations,” *Diam. Relat. Mater.*, vol. 8, no. 7, pp. 1285–1290, 1999.

[11] M. Schöbel *et al.*, “Thermal fatigue damage in monofilament reinforced copper for heat sink applications in divertor elements,” *J. Nucl. Mater.*, vol. 409, no. 3, pp. 225–234, 2011.

[12] S. Kimmig, S. Elgeti, and J. H. You, “Impact of long-term thermal exposure on a SiC fiber-reinforced copper matrix composite,” *J. Nucl. Mater.*, vol. 443, no. 1–3, pp. 386–392, 2013.

[13] G. Pintsuk, S. E. Brünings, J. E. Döring, J. Linke, I. Smid, and L. Xue, “Development of W/Cu-functionally graded materials,” *Fusion Eng. Des.*, vol. 66–68, pp. 237–240, 2003.

[14] Z. J. Zhou, S. X. Song, J. Du, Z. H. Zhong, and C. C. Ge, “Performance of W/Cu FGM

based plasma facing components under high heat load test," *J. Nucl. Mater.*, vol. 363–365, no. 1–3, pp. 1309–1314, 2007.

[15] J. H. You, A. Brendel, S. Nawka, T. Schubert, and B. Kieback, "Thermal and mechanical properties of infiltrated W/CuCrZr composite materials for functionally graded heat sink application," *J. Nucl. Mater.*, vol. 438, no. 1–3, pp. 1–6, 2013.

[16] J. W. Yeh *et al.*, "Nanostructured high-entropy alloys with multiple principal elements: Novel alloy design concepts and outcomes," *Adv. Eng. Mater.*, vol. 6, no. 5, p. 299–303+274, 2004.

[17] B. Cantor, "Multicomponent and high entropy alloys," *Entropy*, vol. 16, no. 9, pp. 4749–4768, 2014.

[18] B. Cantor, I. T. H. Chang, P. Knight, and A. J. B. Vincent, "Microstructural development in equiatomic multicomponent alloys," *Mater. Sci. Eng. A*, vol. 375–377, no. 1–2 SPEC. ISS., pp. 213–218, 2004.

[19] P. Huang and J. Yeh, "Multi-Principal Element Alloys with Improved Oxidation and Wear Resistance for Thermal Spray Coating," *Adv. Eng. Mater.*, vol. 6, no. 1–2, pp. 74–78, 2004.

[20] S. Ranganathan, "Alloyed pleasures: Multimetallic cocktails," *Curr. Sci.*, vol. 85, no. 10, pp. 1404–1406, 2003.

[21] B. S. Murty, J. W. Yeh, and S. Ranganathan, *High Entropy Alloys*. 2014.

[22] M. C. Gao, J. W. Yeh, P. K. Liaw, and Y. Zhang, *High Entropy Alloys: Fundamentals and Applications*. 2016.

[23] Y. Zhang, Y. J. Zhou, J. P. Lin, G. L. Chen, and P. K. Liaw, "Solid-solution phase formation rules for multi-component alloys," *Adv. Eng. Mater.*, vol. 10, no. 6, pp. 534–538, 2008.

[24] Y. Zhang *et al.*, "Microstructures and properties of high-entropy alloys," *Prog. Mater. Sci.*, vol. 61, no. September 2013, pp. 1–93, 2014.

[25] D. A. Porter, K. E. Easterling, and M. Y. Sherif, "Phase Transformations in Metals and Alloys," 3rd ed., 2009, p. 13.

[26] J. W. Yeh, "Alloy design strategies and future trends in high-entropy alloys," *JOM*, vol. 65, no. 12, pp. 1759–1771, 2013.

[27] B. Fultz, "Vibrational thermodynamics of materials," *Prog. Mater. Sci.*, vol. 55, no. 4, pp. 247–352, 2010.

[28] D. B. Miracle, J. D. Miller, O. N. Senkov, C. Woodward, M. D. Uchic, and J. Tiley, "Exploration and development of high entropy alloys for structural applications," *Entropy*, vol. 16, no. 1, pp. 494–525, 2014.

[29] J. W. Yeh, “Recent progress in high-entropy alloys,” *Ann. Chim. Sci. des Mater.*, vol. 31, no. 6, pp. 633–648, 2006.

[30] D. B. Miracle and O. N. Senkov, “A critical review of high entropy alloys and related concepts,” *Acta Mater.*, vol. 122, pp. 448–511, 2017.

[31] X. Wang, H. Xie, L. Jia, and Z. L. Lu, “Effect of Ti, Al and Cu Addition on Structural Evolution and Phase Constitution of FeCoNi System Equimolar Alloys,” *Mater. Sci. Forum*, vol. 724, pp. 335–338, 2012.

[32] O. N. Senkov, G. B. Wilks, J. M. Scott, and D. B. Miracle, “Mechanical properties of Nb25Mo25Ta25W25 and V20Nb20Mo20Ta20W20 refractory high entropy alloys,” *Intermetallics*, vol. 19, no. 5, pp. 698–706, 2011.

[33] N. G. Jones, J. W. Aveson, A. Bhowmik, B. D. Conduit, and H. J. Stone, “On the entropic stabilisation of an Al0.5CrFeCoNiCu high entropy alloy,” *Intermetallics*, vol. 54, pp. 148–153, 2014.

[34] Y. X. Zhuang, H. D. Xue, Z. Y. Chen, Z. Y. Hu, and J. C. He, “Effect of annealing treatment on microstructures and mechanical properties of FeCoNiCuAl high entropy alloys,” *Mater. Sci. Eng. A*, vol. 572, pp. 30–35, 2013.

[35] F. Otto, Y. Yang, H. Bei, and E. P. George, “Relative effects of enthalpy and entropy on the phase stability of equiatomic high-entropy alloys,” *Acta Mater.*, vol. 61, no. 7, pp. 2628–2638, 2013.

[36] J. W. Yeh, S. Y. Chang, Y. Der Hong, S. K. Chen, and S. J. Lin, “Anomalous decrease in X-ray diffraction intensities of Cu-Ni-Al-Co-Cr-Fe-Si alloy systems with multi-principal elements,” *Mater. Chem. Phys.*, vol. 103, no. 1, pp. 41–46, 2007.

[37] R. S. Ganji, P. Sai Karthik, K. Bhanu Sankara Rao, and K. V. Rajulapati, “Strengthening mechanisms in equiatomic ultrafine grained AlCoCrCuFeNi high-entropy alloy studied by micro- and nanoindentation methods,” *Acta Mater.*, vol. 125, pp. 58–68, 2017.

[38] C. L. Lu, S. Y. Lu, J. W. Yeh, and W. K. Hsu, “Thermal expansion and enhanced heat transfer in high-entropy alloys,” *J. Appl. Crystallogr.*, vol. 46, no. 3, pp. 736–739, 2013.

[39] C. W. Tsai, Y. L. Chen, M. H. Tsai, J. W. Yeh, T. T. Shun, and S. K. Chen, “Deformation and annealing behaviors of high-entropy alloy Al0.5CoCrCuFeNi,” *J. Alloys Compd.*, vol. 486, no. 1–2, pp. 427–435, 2009.

[40] C. Y. Hsu, C. C. Juan, W. R. Wang, T. S. Sheu, J. W. Yeh, and S. K. Chen, “On the superior hot hardness and softening resistance of AlCoCrxFeMo0.5Ni high-entropy alloys,” *Mater. Sci. Eng. A*, vol. 528, no. 10–11, pp. 3581–3588, 2011.

[41] P. K. Huang and J. W. Yeh, “Inhibition of grain coarsening up to 1000 ^{o}C in (AlCrNbSiTiV)N superhard coatings,” *Scr. Mater.*, vol. 62, no. 2, pp. 105–108, 2010.

[42] K. Y. Tsai, M. H. Tsai, and J. W. Yeh, “Sluggish diffusion in Co-Cr-Fe-Mn-Ni high-entropy alloys,” *Acta Mater.*, vol. 61, no. 13, pp. 4887–4897, 2013.

[43] W.-R. Wang, W.-L. Wang, S.-C. Wang, Y.-C. Tsai, C.-H. Lai, and J.-W. Yeh, “Effects of Al addition on the microstructure and mechanical property of AlxCoCrFeNi high-entropy alloys,” *Intermetallics*, vol. 26, pp. 44–51, 2012.

[44] O. N. Senkov, G. B. Wilks, D. B. Miracle, C. P. Chuang, and P. K. Liaw, “Refractory high-entropy alloys,” *Intermetallics*, vol. 18, no. 9, pp. 1758–1765, 2010.

[45] Y. Zhang, T. Zuo, Y. Cheng, and P. K. Liaw, “High-entropy alloys with high saturation magnetization, electrical resistivity, and malleability.,” *Sci. Rep.*, vol. 3, p. 1455, 2013.

[46] Y. Zhang and Y. J. Zhou, “Solid Solution Formation Criteria for High Entropy Alloys,” *Mater. Sci. Forum*, vol. 561–565, pp. 1337–1339, 2007.

[47] S. Guo, Q. Hu, C. Ng, and C. T. Liu, “More than entropy in high-entropy alloys: Forming solid solutions or amorphous phase,” *Intermetallics*, vol. 41, pp. 96–103, 2013.

[48] J. M. Zhu, H. M. Fu, H. F. Zhang, A. M. Wang, H. Li, and Z. Q. Hu, “Microstructures and compressive properties of multicomponent AlCoCrFeNiMox alloys,” *Mater. Sci. Eng. A*, vol. 527, no. 26, pp. 6975–6979, 2010.

[49] X. Yang and Y. Zhang, “Prediction of high-entropy stabilized solid-solution in multi-component alloys,” *Mater. Chem. Phys.*, vol. 132, no. 2–3, pp. 233–238, 2012.

[50] Z. Wang, S. Guo, and C. T. Liu, “Phase Selection in High-Entropy Alloys: From Nonequilibrium to Equilibrium,” *Jom*, vol. 66, no. 10, pp. 1966–1972, 2014.

[51] S. Guo, C. Ng, J. Lu, and C. T. Liu, “Effect of valence electron concentration on stability of fcc or bcc phase in high entropy alloys,” *J. Appl. Phys.*, vol. 109, no. 10, 2011.

[52] “Appendix 6 - Crystal Structures and Lattice Parameters of Allotropes of the Metallic Elements,” in *ASM Handbook Volume 3: Alloy Phase Diagrams*, 1992.

[53] “Appendix 3 - Melting and Boiling Points of the Elements at Atmospheric Pressure,” in *ASM Handbook Volume 3: Alloy Phase Diagrams*, 1992.

[54] O. N. Senkov and D. B. Miracle, “Effect of the atomic size distribution on glass forming ability of amorphous metallic alloys,” *Pergamon Mater. Res. Bull.*, vol. 36, pp. 2183–2198, 2001.

[55] S. Guo and C. T. Liu, “Phase stability in high entropy alloys: Formation of solid-solution phase or amorphous phase,” *Prog. Nat. Sci. Mater. Int.*, vol. 21, no. 6, pp. 433–446, 2011.

[56] “Appendix 4 - Allotropic Transformations of the Elements at Atmospheric Pressure,” in *ASM Handbook Volume 3: Alloy Phase Diagrams*, 1992.

[57] I. P. Polmear, *Light Alloys - From Traditional Alloys to Nanocrystals*, 4th ed., vol. 2. 2006.

[58] F. J. Baldenebro-Lopez, J. M. Herrera-Ramírez, S. P. Arredondo-Rea, C. D. Gómez-Esparza, and R. Martínez-Sánchez, “Simultaneous effect of mechanical alloying and arc-melting processes in the microstructure and hardness of an AlCoFeMoNiTi high-entropy alloy,” *J. Alloys Compd.*, vol. 643, pp. S250–S255, 2014.

[59] P. P. Bhattacharjee *et al.*, “Microstructure and texture evolution during annealing of equiatomic CoCrFeMnNi high-entropy alloy,” *J. Alloys Compd.*, vol. 587, pp. 544–552, 2014.

[60] A. K. Mishra, S. Samal, and K. Biswas, “Solidification behaviour of Ti-Cu-Fe-Co-Ni high entropy alloys,” *Trans. Indian Inst. Met.*, vol. 65, no. 6, pp. 725–730, 2012.

[61] D. H. Xiao *et al.*, “Microstructure, mechanical and corrosion behaviors of AlCoCuFeNi-(Cr,Ti) high entropy alloys,” *Mater. Des.*, vol. 116, pp. 438–447, 2016.

[62] Z. G. Zhu, K. H. Ma, Q. Wang, and C. H. Shek, “Compositional dependence of phase formation and mechanical properties in three CoCrFeNi-(Mn/Al/Cu) high entropy alloys,” *Intermetallics*, vol. 79, pp. 1–11, 2016.

[63] Y. Zhang, S. G. Ma, and J. W. Qiao, “Morphology transition from dendrites to equiaxed grains for AlCoCrFeNi high-entropy alloys by copper mold casting and bridgman solidification,” *Metall. Mater. Trans. A Phys. Metall. Mater. Sci.*, vol. 43, no. 8, pp. 2625–2630, 2012.

[64] M. J. Yao, K. G. Pradeep, C. C. Tasan, and D. Raabe, “A novel, single phase, non-equiatomic FeMnNiCoCr high-entropy alloy with exceptional phase stability and tensile ductility,” *Scr. Mater.*, vol. 72–73, pp. 5–8, 2014.

[65] S. Singh, N. Wanderka, B. S. Murty, U. Glatzel, and J. Banhart, “Decomposition in multi-component AlCoCrCuFeNi high-entropy alloy,” *Acta Mater.*, vol. 59, no. 1, pp. 182–190, 2011.

[66] K. M. Youssef, A. J. Zaddach, C. Niu, D. L. Irving, and C. C. Koch, “A Novel Low-Density, High-Hardness, High-entropy Alloy with Close-packed Single-phase Nanocrystalline Structures,” *Mater. Res. Lett.*, vol. 3, no. 2, pp. 95–99, 2015.

[67] S. Varalakshmi, M. Kamaraj, and B. S. Murty, “Synthesis and characterization of nanocrystalline AlFeTiCrZnCu high entropy solid solution by mechanical alloying,” *J. Alloys Compd.*, vol. 460, no. 1–2, pp. 253–257, 2008.

[68] Y. L. Chen, Y. H. Hu, C. A. Hsieh, J. W. Yeh, and S. K. Chen, “Competition between elements during mechanical alloying in an octonary multi-principal-element alloy system,” *J. Alloys Compd.*, vol. 481, no. 1–2, pp. 768–775, 2009.

[69] S. Varalakshmi, M. Kamaraj, and B. S. Murty, “Formation and stability of equiatomic and

nonequiatomic nanocrystalline CuNiCoZnAlTi high-entropy alloys by mechanical alloying," *Metall. Mater. Trans. A Phys. Metall. Mater. Sci.*, vol. 41, no. 10, pp. 2703–2709, 2010.

[70] Y. L. Chen *et al.*, "Alloying behavior of binary to octonary alloys based on Cu-Ni-Al-Co-Cr-Fe-Ti-Mo during mechanical alloying," *J. Alloys Compd.*, vol. 477, no. 1–2, pp. 696–705, 2009.

[71] S. Varalakshmi, M. Kamaraj, and B. S. Murty, "Processing and properties of nanocrystalline CuNiCoZnAlTi high entropy alloys by mechanical alloying," *Mater. Sci. Eng. A*, vol. 527, no. 4–5, pp. 1027–1030, 2010.

[72] R. Sriharitha, B. S. Murty, and R. S. Kottada, "Alloying, thermal stability and strengthening in spark plasma sintered AlxCoCrCuFeNi high entropy alloys," *J. Alloys Compd.*, vol. 583, no. January, pp. 419–426, 2014.

[73] S. Praveen, B. S. Murty, and R. S. Kottada, "Phase evolution and densification behavior of nanocrystalline multicomponent high entropy alloys during spark plasma sintering," *Jom*, vol. 65, no. 12, pp. 1797–1804, 2013.

[74] H. P. Chou, Y. S. Chang, S. K. Chen, and J. W. Yeh, "Microstructure, thermophysical and electrical properties in AlxCoCrFeNi (0<x<2) high-entropy alloys," *Mater. Sci. Eng. B Solid-State Mater. Adv. Technol.*, vol. 163, no. 3, pp. 184–189, 2009.

[75] S. Q. Xia, X. Yang, T. F. Yang, S. Liu, and Y. Zhang, "Irradiation Resistance in Al x CoCrFeNi High Entropy Alloys," *JOM*, vol. 67, no. 10, pp. 3–7, 2015.

[76] F. Granberg *et al.*, "Mechanism of Radiation Damage Reduction in Equiatomic Multicomponent Single Phase Alloys," *Phys. Rev. Lett.*, vol. 116, no. 13, pp. 1–8, 2016.

[77] T. Egami, M. Ojha, O. Khorgolkhuu, D. M. Nicholson, and G. M. Stocks, "Local Electronic Effects and Irradiation Resistance in High-Entropy Alloys," *Jom*, vol. 67, no. 10, pp. 2345–2349, 2015.

[78] T. Nagase *et al.*, "Electron-irradiation-induced structural change in Zr-Hf-Nb alloy," *Intermetallics*, vol. 26, pp. 122–130, 2012.

[79] T. Egami, W. Guo, P. D. Rack, and T. Nagase, "Irradiation resistance of multicomponent alloys," *Metall. Mater. Trans. A Phys. Metall. Mater. Sci.*, vol. 45, no. 1, pp. 180–183, 2014.

[80] M. C. Gao and D. E. Alman, "Searching for Next Single-Phase High-Entropy Alloy Compositions," *Entropy*, vol. 15, pp. 4504–4519, 2004.

[81] Q. Li *et al.*, "Ti50Cu23Ni20Sn7 bulk metallic glasses prepared by mechanical alloying and spark-plasma sintering," *J. Mater. Process. Technol.*, vol. 209, no. 7, pp. 3285–3288, 2009.

[82] C. Suryanarayana, "Mechanical alloying and milling," *Prog. Mater. Sci.*, vol. 46, no. 1–2,

pp. 1–184, 2001.

[83] F. Hadef and A. Otmani, “Mechanical Alloying/Milling,” in *Handbook of Mechanical Nanostructuring*, Weinheim, Germany: Wiley-VCH Verlag GmbH & Co. KGaA, 2015, pp. 263–276.

[84] M. Omori, “Sintering , consolidation , reaction and crystal growth by the spark plasma system (SPS),” *Mater. Sci. Eng. A*, vol. 287, pp. 183–188, 2000.

[85] Z. Zhaohui, W. Fuchi, W. Lin, L. Shukui, and S. Osamu, “Sintering mechanism of large-scale ultrafine-grained copper prepared by SPS method,” *Mater. Lett.*, vol. 62, no. 24, pp. 3987–3990, 2008.

[86] S. Diouf and A. Molinari, “Densification mechanisms in spark plasma sintering: Effect of particle size and pressure,” *Powder Technol.*, vol. 221, pp. 220–227, 2012.

[87] X. Song, X. Liu, and J. Zhang, “Neck formation and self-adjusting mechanism of neck growth of conducting powders in spark plasma sintering,” *J. Am. Ceram. Soc.*, vol. 89, no. 2, pp. 494–500, 2006.

[88] Z. H. Zhang, Z. F. Liu, J. F. Lu, X. B. Shen, F. C. Wang, and Y. D. Wang, “The sintering mechanism in spark plasma sintering - Proof of the occurrence of spark discharge,” *Scr. Mater.*, vol. 81, pp. 56–59, 2014.

[89] http://www.srim.org, “SRIM 2013 Software Package.” .

[90] J. F. Ziegler, M. D. Ziegler, and J. P. Biersack, “SRIM - The stopping and range of ions in matter (2010),” *Nucl. Instruments Methods Phys. Res. Sect. B Beam Interact. with Mater. Atoms*, vol. 268, no. 11–12, pp. 1818–1823, 2010.

[91] Oxford-instruments, “Oxford INCA Energy Dispersive Spectrometer (EDS) - Training Guide.” [Online]. Available: http://chanl.unc.edu/assets/pdf_files/operations/spectroscopy/EDS_training.pdf. [Accessed: 16-Oct-2017].

[92] O. X. Data, “X-ray data booklet,” *Berkeley Nat Lab*, vol. 8, no. 4. p. 1125, 2001.

[93] Http://www.icdd.com, “ICDD PDF-2 DATABASE.” .

[94] W. Kraus and G. Nolze, “Powder Cell for Windows, Version 2.2, Federal Institute for Materials Research and Testing.” Berlin, 1999.

[95] “Channel5.” [Online]. Available: http://www.oxinst.eu/products/microanalysis/ebsd/ebsd-acquisition software/Pages/channel5.aspx.

[96] A. P. Gonçalves *et al.*, “Peculiarities of U-based Laves Phases,” *IOP Conf. Ser. Mater. Sci. Eng.*, vol. 9, no. 1, p. 12, 2010.

[97] A. K. Singh, N. Kumar, A. Dwivedi, and A. Subramaniam, “A geometrical parameter for the formation of disordered solid solutions in multi-component alloys,” *Intermetallics*, vol. 53, 2014.

[98] M. H. Tsai *et al.*, “Morphology, structure and composition of precipitates in Al 0.3CoCrCu 0.5FeNi high-entropy alloy,” *Intermetallics*, vol. 32, pp. 329–336, 2013.

[99] X. F. Wang, Y. Zhang, Y. Qiao, and G. L. Chen, “Novel microstructure and properties of multicomponent CoCrCuFeNiTix alloys,” *Intermetallics*, vol. 15, no. 3, pp. 357–362, 2007.

[100] C. C. Tung, J. W. Yeh, T. tsung Shun, S. K. Chen, Y. S. Huang, and H. C. Chen, “On the elemental effect of AlCoCrCuFeNi high-entropy alloy system,” *Mater. Lett.*, vol. 61, no. 1, pp. 1–5, 2007.

[101] ASM International Alloy Phase Diagram and Handbook Comittee, *ASM Handbook Volume 3: Alloy Phase Diagrams*, vol. 3. 1992.

[102] Y. Dong, Y. Lu, J. Kong, J. Zhang, and T. Li, “Microstructure and mechanical properties of multi-component AlCrFeNiMo x high-entropy alloys,” *J. Alloys Compd.*, vol. 573, pp. 96–101, 2013.

[103] A. Takeuchi and A. Inoue, “Classification of Bulk Metallic Glasses By Atomic Size Difference, Heat of Mixing and Period of Constituent Elements and Its Application To Characterization of the Main Alloying Element,” *Mater. Trans.*, vol. 46, no. 12, pp. 2817–2829, 2005.

[104] M.-H. Tsai, K.-Y. Tsai, C.-W. Tsai, C. Lee, C.-C. Juan, and J.-W. Yeh, “Criterion for Sigma Phase Formation in Cr- and V-Containing High-Entropy Alloys,” *Mater. Res. Lett.*, vol. 1, no. 4, pp. 207–212, 2013.

[105] C. C. Juan *et al.*, “On microstructure and mechanical performance of AlCoCrFeMo0.5Nix high-entropy alloys,” *Intermetallics*, vol. 32, pp. 401–407, 2013.

[106] J. M. Zhu, H. F. Zhang, H. M. Fu, A. M. Wang, H. Li, and Z. Q. Hu, “Microstructures and compressive properties of multicomponent AlCoCrCuFeNiMox alloys,” *J. Alloys Compd.*, vol. 497, no. 1–2, pp. 52–56, 2010.

[107] T. T. Shun, L. Y. Chang, and M. H. Shiu, “Microstructures and mechanical properties of multiprincipal component CoCrFeNiTix alloys,” *Mater. Sci. Eng. A*, vol. 556, pp. 170–174, 2012.

[108] B. Predel, “Cr-Mo (Chromium-Molybdenum),” in *Cr-Cs – Cu-Zr*, Berlin/Heidelberg: Springer-Verlag, pp. 1–5.

[109] T. T. Shun, L. Y. Chang, and M. H. Shiu, “Microstructures and mechanical properties of multiprincipal component CoCrFeNiTix alloys,” *Mater. Sci. Eng. A*, vol. 556, pp. 170–174, 2012.

[110] Y. J. Zhou, Y. Zhang, Y. L. Wang, and G. L. Chen, “Solid solution alloys of AlCoCrFeNiTix with excellent room-temperature mechanical properties,” *Appl. Phys. Lett.*, vol. 90, no. 18, p. 181904, 2007.

[111] C. T. Liu, J. H. Zhu, M. P. Brady, C. G. McKamey, and L. M. Pike, “Physical metallurgy and mechanical properties of transition- metal Laves phase alloys,” *Intermetallics*, vol. 8, no. 9–11, pp. 1119–1129, 2000.

[112] K. Chen, S. Allen, and J. Livingston, “Factors Affecting the Room-Temperature Mechanical Properties of $TiCr_2$-Base Laves Phase Alloys,” *Mater. Sci. Eng. A*, vol. 242, no. 1–2, pp. 162–173, 1998.

[113] T. Velikanova and M. Turchanin, “Copper – Iron – Titanium,” in *Group*, vol. 11, 2008, pp. 27–50.

[114] L. N. Series, “Ternary System Fe-Mo-Ti,” in *Ternary Steel Systems: Phase Diagrams and Phase Transition Data*, Berlin, Heidelberg: Springer Berlin Heidelberg, 2015, pp. 152–161.

[115] C.-J. Tong *et al.*, “Microstructure characterization of Al x CoCrCuFeNi high-entropy alloy system with multiprincipal elements,” *Metall. Mater. Trans. A*, vol. 36, no. 4, pp. 881–893, 2005.

[116] L. H. Wen, H. C. Kou, J. S. Li, H. Chang, X. Y. Xue, and L. Zhou, “Effect of aging temperature on microstructure and properties of AlCoCrCuFeNi high-entropy alloy,” *Intermetallics*, vol. 17, no. 4, pp. 266–269, 2009.

[117] U. S. Hsu, U. D. Hung, J. W. Yeh, S. K. Chen, Y. S. Huang, and C. C. Yang, “Alloying behavior of iron, gold and silver in AlCoCrCuNi-based equimolar high-entropy alloys,” *Mater. Sci. Eng. A*, vol. 460–461, pp. 403–408, 2007.

[118] B. Predel, “Cu-Ti (Copper-Titanium),” in *Cr-Cs – Cu-Zr*, vol. 5, no. 1963, Berlin/Heidelberg: Springer-Verlag, 1984, pp. 1–7.

[119] L. Y. Chen, C. H. Li, K. Wang, H. Q. Dong, X. G. Lu, and W. Z. Ding, “Thermodynamic modeling of Ti-Fe-Cr ternary system,” *Calphad Comput. Coupling Phase Diagrams Thermochem.*, vol. 56, pp. 160–168, 2017.

[120] G. Zhou, D. Zeng, and Z. Liu, “Phase equilibria in the Fe-Ti-V system at 1023 K,” *J. Alloys Compd.*, vol. 490, no. 1–2, pp. 463–467, 2010.

[121] C. Li, J. L. Hoe, and P. Wu, “Empirical correlation between melting temperature and cohesive energy of binary Laves phases,” *J. Phys. Chem. Solids*, vol. 64, no. 2, pp. 201–212, 2003.

[122] J. H. Zhu, P. K. Liaw, and C. T. Liu, “Effect of electron concentration on the phase stability of NbCr 2 -based Laves phase alloys,” *Mater. Sci. Eng. A*, vol. 239–240, pp. 260–264, 1997.

[123] K. Young, M. A. Fetcenko, F. Li, T. Ouchi, and J. Koch, “Effect of vanadium substitution in C14 Laves phase alloys for NiMH battery application,” *J. Alloys Compd.*, vol. 468, no. 1–2, pp. 482–492, 2009.

[124] B. S. Li, Y. P. Wang, M. X. Ren, C. Yang, and H. Z. Fu, “Effects of Mn, Ti and V on the microstructure and properties of AlCrFeCoNiCu high entropy alloy,” *Mater. Sci. Eng. A*, vol. 498, no. 1–2, pp. 482–486, 2008.

[125] S. Guo, C. Ng, Z. Wang, and C. T. Liu, “Solid solutioning in equiatomic alloys: Limit set by topological instability,” *J. Alloys Compd.*, vol. 583, pp. 410–413, 2014.

[126] M. Fujitsuka, B. Tsuchiya, I. Mutoh, T. Tanabe, and T. Shikama, “Effect of neutron irradiation on thermal diffusivity of tungsten–rhenium alloys,” *J. Nucl. Mater.*, vol. 283–287, pp. 1148–1151, 2000.

[127] M. Rohde *et al.*, “Intercomparison of thermal diffusivity measurements on CuCrZr and PMMA,” *High Temp. - High Press.*, vol. 42, no. 6, pp. 469–474, 2013.

[128] S. Praveen, B. S. Murty, and R. S. Kottada, “Alloying behavior in multi-component AlCoCrCuFe and NiCoCrCuFe high entropy alloys,” *Mater. Sci. Eng. A*, vol. 534, pp. 83–89, 2012.

[129] S. Mridha, S. Samal, P. Y. Khan, K. Biswas, and Govind, “Processing and consolidation of nanocrystalline Cu-Zn-Ti-Fe-Cr high-entropy alloys via mechanical alloying,” *Metall. Mater. Trans. A Phys. Metall. Mater. Sci.*, vol. 44, no. 10, pp. 4532–4541, 2013.

[130] K. G. Pradeep, N. Wanderka, P. Choi, J. Banhart, B. S. Murty, and D. Raabe, “Atomic-scale compositional characterization of a nanocrystalline AlCrCuFeNiZn high-entropy alloy using atom probe tomography,” *Acta Mater.*, vol. 61, no. 12, pp. 4696–4706, 2013.

[131] R. Sriharitha, B. S. Murty, and R. S. Kottada, “Phase formation in mechanically alloyed AlxCoCrCuFeNi (x = 0.45, 1, 2.5, 5 mol) high entropy alloys,” *Intermetallics*, vol. 32, pp. 119–126, 2013.

[132] H. Bakker, G. F. Zhou, and H. Yang, “Mechanically driven disorder and phase transformations in alloys,” *Prog. Mater. Sci.*, vol. 39, no. 3, pp. 159–241, 1995.

[133] N. Karpe, K. K. Larsen, and J. Bo/ttiger, “Phase formation induced by ion irradiation and electrical resistivity of aluminum–3 d -transition-metal alloys,” *Phys. Rev. B*, vol. 46, no. 5, pp. 2686–2692, Aug. 1992.